



Multi-satellite sensor study on precipitation-induced emission pulses of NO_x from soils in semi-arid ecosystems

Jan Zörner¹, Marloes Penning de Vries¹, Steffen Beirle¹, Holger Sihler^{1,3}, Patrick R. Veres^{2,a}, Jonathan Williams², and Thomas Wagner¹

¹Satellite Remote Sensing Group, Max Planck Institute for Chemistry, Mainz, Germany

²Atmospheric Chemistry Department, Max Planck Institute for Chemistry, Mainz, Germany

³Institute of Environmental Physics, University of Heidelberg, Heidelberg, Germany

^anow at: NOAA Earth System Research Laboratory, Boulder, CO, USA

Correspondence to: Jan Zörner (jan.zoerner@mpic.de)

Received: 29 January 2016 – Published in Atmos. Chem. Phys. Discuss.: 25 February 2016

Revised: 27 June 2016 – Accepted: 10 July 2016 – Published: 29 July 2016

Abstract. We present a top-down approach to infer and quantify rain-induced emission pulses of NO_x ($\equiv \text{NO} + \text{NO}_2$), stemming from biotic emissions of NO from soils, from satellite-borne measurements of NO_2 . This is achieved by synchronizing time series at single grid pixels according to the first day of rain after a dry spell of prescribed duration. The full track of the temporal evolution several weeks before and after a rain pulse is retained with daily resolution. These are needed for a sophisticated background correction, which accounts for seasonal variations in the time series and allows for improved quantification of rain-induced soil emissions. The method is applied globally and provides constraints on pulsed soil emissions of NO_x in regions where the NO_x budget is seasonally dominated by soil emissions.

We find strong peaks of enhanced NO_2 vertical column densities (VCDs) induced by the first intense precipitation after prolonged droughts in many semi-arid regions of the world, in particular in the Sahel. Detailed investigations show that the rain-induced NO_2 pulse detected by the OMI (Ozone Monitoring Instrument), GOME-2 and SCIAMACHY satellite instruments could not be explained by other sources, such as biomass burning or lightning, or by retrieval artefacts (e.g. due to clouds).

For the Sahel region, absolute enhancements of the NO_2 VCDs on the first day of rain based on OMI measurements 2007–2010 are on average 4×10^{14} molec cm^{-2} and exceed 1×10^{15} molec cm^{-2} for individual grid cells. Assuming a NO_x lifetime of 4 h, this corresponds to soil NO_x emissions in the range of 6 up to 65 ng $\text{Nm}^{-2} \text{s}^{-1}$, which is

in good agreement with literature values. Apart from the clear first-day peak, NO_2 VCDs are moderately enhanced (2×10^{14} molec cm^{-2}) compared to the background over the following 2 weeks, suggesting potential further emissions during that period of about 3.3 ng $\text{Nm}^{-2} \text{s}^{-1}$. The pulsed emissions contribute about 21–44 % to total soil NO_x emissions over the Sahel.

1 Introduction

Nitrogen oxides ($\text{NO}_x \equiv \text{NO} + \text{NO}_2$) play an important role in tropospheric chemistry. They are key catalysts in chemical processes generating and destroying ozone (O_3) (Crutzen, 1995; Crutzen and Lelieveld, 2001; Seinfeld and Pandis, 2006). Ambient mixing ratios of NO_x and volatile organic compounds (VOCs) determine whether tropospheric O_3 is formed or consumed (Chameides et al., 1992; Crutzen and Lelieveld, 2001). In polluted conditions with high NO_x , through the reaction of nitric oxide (NO) with the hydroperoxyl radical (HO_2), NO_x is also involved in the production of the hydroxyl radical (OH) and, thus, impacts the tropospheric oxidizing capacity (Monks, 2005). During daytime, NO_x is mainly removed from the atmosphere by oxidation with OH producing nitric acid (HNO_3) (Jacob, 1999; Monks, 2005), which is an important component of acid deposition and contributes to nitrate aerosol formation (Bassett and Seinfeld, 1983). Furthermore, NO_x is also removed by NO_2 deposition on vegetated surfaces (Ganzeveld et al., 2002). At

night, N₂O₅ hydrolysis on aerosol surfaces is the dominant sink of NO_x (Jacob, 1999).

While anthropogenic activity such as fossil-fuel combustion is the largest source of NO_x, there are also important natural sources including natural biomass burning from forest fires, lightning and microbial processes in soils. Soil emissions of NO_x (sNO_x) constitute an estimated fraction of ≈ 15 % of total NO_x on a global basis (Warneck and Williams, 2012; Hudman et al., 2012) and may even dominate the local NO_x budget in non-industrialized regions like remote tropical and agricultural areas (Yienger and Levy, 1995; Steinkamp et al., 2009). Bottom-up approaches using global chemistry models suggest global fluxes between 4 and 15 Tg N yr⁻¹ with uncertainties of up to 5–10 Tg N yr⁻¹ (e.g. Yienger and Levy, 1995; Steinkamp and Lawrence, 2011; Hudman et al., 2012; Vinken et al., 2014, and references therein). Satellite constrained top-down approaches hint at regional underestimations of sNO_x of a factor of 2 and more (Jaeglé et al., 2004; Wang et al., 2007; Boersma et al., 2008; Zhao and Wang, 2009; Vinken et al., 2014). Thus, global emissions of sNO_x remain uncertain.

Emissions of NO_x from natural and anthropogenically influenced soils are mainly driven by microbial activity within the top soil layer and associated chemical reactions (Conrad, 1996). Primarily, two important groups of micro-organisms, nitrifiers and denitrifiers, are involved in processes related to the turnover of nutrients in the soil (Pilegaard, 2013; Behrendt et al., 2014). They are directly responsible for the corresponding processes of (i) nitrification, the biological oxidation of nitrogen compounds, typically the oxidation of soil ammonium (NH₄⁺) to nitrate (NO₃⁻) and (ii) denitrification, the reduction of nitrate by microbes to gaseous products, i.e. N₂O and finally N₂. NO is a gaseous by-product of both processes and once released reacts with ambient O₃, to form NO₂ and oxygen (O₂) within minutes. Findings from Oswald et al. (2013) suggest that gaseous nitrous acid (HONO), which is rapidly photolysed to NO, is also emitted from soils.

Most soil emissions of NO in semi-arid areas are linked to microbial processes, but some chemical (abiotic) formation processes of NO are known to exist, which are more important for acidic soils with high nitrite (NO₂⁻) concentrations (Davidson, 1992b). Such soils are found in humid regions, i.e. the humid tropical belt and the northern temperate zone, where soil leaching removes alkaline material and associated salts from the soil profiles leading to pH values of less than 5.5 (Merry, 2009). Emissions of nitrogen-containing gases, such as NO, N₂ and N₂O increase dramatically in soils with enhanced nitrogen availability due to the presence of N-fixing microbial species and plants (Virginia et al., 1982; van Groenigen et al., 2015). In semi-arid areas with sparse vegetation cover, surfaces are covered by a variety of communities of cyanobacteria, algae, lichens, mosses, microfungi, and other bacteria in differing proportions (Belnap and Lange, 2001; Barger et al., 2005). Associated organisms within these biological crusted soils fix atmospheric N₂

and, thus, raise the nitrogen availability in the soil (Evans and Ehleringer, 1993). Barger et al. (2005) found varying rates of soil NO fluxes from biologically crusted soils that differed in their nitrogen fixation potentials. Recent findings from Weber et al. (2015) suggest that dryland emissions of reactive nitrogen are largely driven by biocrusts rather than the underlying soil and strongly depend on the soil water content (SWC), i.e. precipitation events. Throughout this study, for simplicity all emissions from soils and biocrusts are referred to as sNO_x.

Soil emissions of trace gases depend on a wide range of ambient environmental conditions such as soil type, soil moisture, temperature, pH-Value and nitrogen content (Conrad, 1996; Ludwig et al., 2001; Meixner and Yang, 2006; Oswald et al., 2013). Also agricultural management practices, such as soil cultivation, fertilization and irrigation can strongly affect the fluxes (Bouwman et al., 2002). In remote regions like the Sahel, where synthetic fertilizer is limited, manure plays a prominent role in the fertilization of agricultural fields and can contribute significantly to the input of organic nitrogen into the soil (Schlecht and Hiernaux, 2004; Delon et al., 2010). The effective NO_x fluxes from soils to the atmosphere are potentially offset by “canopy reduction” where nitrogen oxides are quickly deposited on available vegetation surfaces (Ganzeveld et al., 2002). During the dry season in tropical ecosystems soils accumulate inorganic nitrogen through N-fixing micro-organisms. Subsequently, water-stressed microbes trapped in the soil become activated by the first rain event of the wet season and release NO as a by-product of nitrogen consumption (Davidson, 1992a). Rain-induced pulsing events of NO_x emissions were observed in situ and by laboratory measurements of soil samples (e.g. Williams et al., 1987, 1992; Johansson and Sanhueza, 1988; Levine et al., 1996; Scholes et al., 1997; Kim et al., 2012; Wang et al., 2015). Pulsed emissions of sNO_x occurring at the transition phase between the dry and wet season, were previously also observed from space (Jaeglé et al., 2004; Bertram et al., 2005; Hudman et al., 2012) in the Sahel region. Hudman et al. (2012) showed that intense but short events of soil emissions, i.e. pulsed emissions, at the start of the wet season after a prolonged dry spell represent a large fraction of annual soil emissions in the Sahel region. As noted by Hudman et al. (2012) further research needs to be done to verify that the observed pulses by OMI (Ozone Monitoring Instrument) are not biased by the retrieval algorithm.

The main objective of this study is to quantify precipitation-induced short-term enhancements in soil emissions of NO_x, which show peak emissions on the scale of 1–3 days, from space-based instruments in semi-arid regions in the world. This is achieved by investigating the evolution of tropospheric NO₂ column densities from multiple satellite sensors before and after the first rainfall events on the onset of the wet season.

We introduce an optimized algorithm that synchronizes and averages multiple time series of atmospheric variables either from one location only, or from individual grid pixels, by aligning them on a relative timescale to each other. Our algorithm enhances the basic approach described by Hudman et al. (2012) with several features: (i) performing the analysis globally with (ii) high spatial resolution, which is both achieved by expanding the time span of the study to several years (2007 to 2010) enabling an investigation of single grid pixels of 0.25° with reasonable statistics. (iii) The full track of the temporal evolution several weeks before and after a rain pulse is retained with daily resolution. (iv) By intercomparing measurements of NO₂ from multiple satellite instruments it is possible to quantify potential measurement artefacts and investigate the impact of different retrieval algorithms. Furthermore, sensitivity studies are conducted in order to evaluate the impact of the a priori assumptions on thresholds for daily rainfall, i.e. the definition of drought, and its requested duration.

Our approach is a purely *top-down* method, in the sense that satellite data of trace gases are exclusively used to describe and quantify phenomena taking place on the Earth's surface and atmosphere. It is, therefore, extremely important to consider natural processes in the atmosphere that could trigger soil emissions or may affect the retrieved NO₂ column densities in other ways. In order to achieve this we incorporate total columns of water vapour, humidity, temperature and wind directions in our analysis to assess the prevailing meteorology. To verify that the observed responses in the trace gas column densities reflect the impact of emission fluxes from the soil, possible interferences from other parameters, e.g. fires, modified cloud fractions, coincidences with lightning events and horizontal transport from polluted regions, are also investigated.

Veres et al. (2014) found in laboratory experiments that also several VOCs including HCHO exhibit pulsed emissions when dry soils are first wetted. Our study, hence, also addresses the question whether HCHO emissions from semi-arid soils can be observed from satellite-borne sensors.

In contrast to previous satellite studies, our study makes a clear distinction between (i) pulsed emissions, which show strong gradients on a day-to-day scale triggered by a singular precipitation event and (ii) background emissions, which are not directly affected or could not be unambiguously related to a strong precipitation pulse. This facilitates the assessment of the contribution from single sNO_x pulses additionally to background levels.

The paper is organized as follows: in Sect. 2, all data products used within this study are presented. In Sect. 3, the basic algorithm used for averaging the time series of environmental parameters along a relative time axis around the first day of precipitation is described. In Sect. 4, this approach is then applied to areas with different spatial extents. We first perform an analysis on a global scale to delineate regions that show pronounced features in sNO_x in response to the first rain after

a prolonged dry spell. In a second step, we focus on Africa and the Sahel region, in specific, and separate the analysis for different seasons. For this region, we investigate fundamental relationships between soil emissions and some of their governing parameters, i.e. soil moisture content, temperature, air humidity. Within this analysis possible interferences from other parameters are also investigated, and detailed sensitivity studies are conducted. In Sect. 5, sNO_x emissions are inferred from the NO₂ VCDs based on a sophisticated background correction. A list of acronyms for commonly used instruments and products in this paper is provided in Table 1.

2 Data

2.1 Satellite observations of trace gases

Vertical column densities (VCDs) of NO₂ and HCHO can be retrieved from nadir-viewing satellite instruments, by analysing solar backscatter radiances in the UV–VIS (ultraviolet–visible) spectral range. Differential Optical Absorption Spectroscopy (DOAS; Platt and Stutz, 2008), which exploits characteristic narrow absorption structures, is typically used for the analysis.

Tropospheric VCDs are usually derived in a multi-step process (e.g. Boersma et al., 2004, 2007; De Smedt et al., 2008, 2012). First, total slant column densities (SCDs) are retrieved, i.e. the integrated concentrations along the effective light path, by fitting the measured spectrum with a model taking into account all other absorbers in the atmosphere. Second, tropospheric SCDs are derived by subtracting the stratospheric column (NO₂) or a latitude-dependent bias estimated over the Pacific (HCHO). Third, the tropospheric SCDs are then translated to tropospheric VCDs. The conversion of SCDs to VCDs is usually performed by dividing the SCDs by a so-called air mass factor (AMF) (Solomon et al., 1987). The AMF is derived from radiative transfer simulations taking into account information of ground albedo, aerosols and clouds, the vertical profile of the trace gas and the satellite viewing geometry (e.g. Palmer et al., 2001; Richter and Burrows, 2002; Martin, 2003).

Except for very low tropospheric trace gas amounts, the tropospheric AMF dominates the uncertainty of tropospheric trace gas observations from space, e.g. caused by insufficient knowledge of the trace gas profiles, aerosols, cloud properties and cloud cover (Boersma et al., 2004). For observations of trace gases in the boundary layer, which are the focus of this study, the main effect of clouds is that they shield the atmosphere below. Thus, in the presence of clouds the retrieved trace gas absorptions (SCDs) are usually decreased compared to clear-sky conditions. During the conversion to VCDs, the AMF compensates for this effect, which, however, might lead to over- or underestimations of the trace gas column densities if the state of the atmosphere is not known precisely. As the transition between days with and

Table 1. List of acronyms for commonly used instruments and products in this paper.

Abbreviation	Name	References
CMORPH	CPC (Climate Prediction Center) MORPHing technique	Joyce et al. (2004)
DOMINO	Derivation of OMI tropospheric NO ₂ project (v2.0)	Boersma et al. (2011)
ECMWF	European Centre for Medium-Range Weather Forecasts	Dee et al. (2011)
FRESCO+	Fast Retrieval Scheme for Clouds from the Oxygen A band	Wang et al. (2008)
GOME	Global Ozone Monitoring Experiment	Burrows et al. (1999)
GOME-2	Global Ozone Monitoring Experiment-2	Callies et al. (2000); Munro et al. (2006, 2016)
MERIS	MEDium Resolution Imaging Spectrometer	Rast et al. (1999)
MODIS	Moderate Resolution Imaging Spectroradiometer	Kaufman et al. (1998)
OMCLDO2	Cloud Pressure and Fraction using O ₂ -O ₂ absorption	Acarreta et al. (2004)
OMI	Ozone Monitoring Instrument	Levelt et al. (2000, 2006)
PERSIANN	Precipitation Estimation from Remotely Sensed Information using Artificial Neural Networks	Sorooshian et al. (2000)
SCIAMACHY	SCanning Imaging Absorption spectroMeter for Atmospheric CHartography	Bovensmann et al. (1999)
SMMR	Scanning Multi-channel Microwave Radiometer	Gloersen and Barath (1977)
SSM/I	Special Sensor Microwave Imager	Wentz and Spencer (1998); Wentz (2013)
TMI	TRMM Microwave Imager	Wentz et al. (2001)
TMPA	Tropical Rainfall Measuring Mission Multisatellite Precipitation Analysis	Huffman et al. (2007)
TRMM	Tropical Rainfall Measuring Mission	Simpson et al. (1996); Huffman et al. (2007)
TROPOMI	TROPOspheric Monitoring Instrument	Veefkind et al. (2012)
WWLLN	World Wide Lightning Location Network	Dowden et al. (2002); Lay et al. (2004); Rodger et al. (2006)

without precipitation generally corresponds to a change in cloud cover, cloud effects need to be investigated. Therefore, satellite measurements retrieved under low and high cloud fractions are studied in detail using cloud information, derived from FRESCO+ (Wang et al., 2008) for GOME-2 and SCIAMACHY and OMCLDO2 (Acarreta et al., 2004) for OMI.

2.2 Satellite instruments and trace gas products

SCIAMACHY (Bovensmann et al., 1999) aboard the ENVISAT satellite was operated from 2002 to 2012. It had a ground pixel size of about 30 km × 60 km (VIS) to 30 km × 120 km (UV). GOME-2 (Callies et al., 2000; Munro et al., 2006) aboard ESA's METOP-A satellite, launched in 2007, has a ground pixel size of about 40 km × 80 km. OMI (Levelt et al., 2000, 2006) on NASA's Aura platform, which was launched in 2004 has a ground pixel size of 13 km × 24 km at nadir and increasing pixel sizes to the far ends of the 2600 km wide swath. In our study, the two outermost pixels are screened out to remove the pixels with the largest viewing angles and lowest spatial resolution. The local overpass times for the three satellite instruments at the Equator are about 09:30 a.m. for GOME-2, 10:00 a.m. for SCIAMACHY and 01:30 p.m. LT for OMI.

For NO₂, the products GOME-2 TM4-NO2A version 2.3, SCIAMACHY TM4-NO2A version 2.3 and OMI DOMINO version 2.0.1 are used (Boersma et al., 2004, 2011). For HCHO the products GOME-2 version 12, SCIAMACHY version 12 and OMI version 14 are used (De Smedt et al., 2012). Data products are provided freely by the Tropospheric Emission Monitoring Internet Service (TEMIS) via <http://www.temis.nl/>.

Differences among the trace gas data products from the three satellite instruments are expected due to, among others, the calculation of the AMF, their different ground pixel size, local overpass time, cloud products used, the diurnal cycle of cloud conditions and the covered time period. Furthermore, the diurnal cycle of the instantaneous NO_x lifetime and emissions might also cause systematic differences between SCIAMACHY and GOME-2 on the one hand, and OMI on the other.

Uncertainties of tropospheric NO₂ VCDs result mainly from uncertainties of the stratospheric correction (about 2 × 10¹⁴ molec cm⁻²) and tropospheric AMFs (about 35–60 %) (Boersma et al., 2004).

2.3 Precipitation

The estimation of precipitation on a daily global scale is facilitated through the combination of radar, passive microwave, VIS and infrared (IR) sensors aboard low-Earth orbiting as well as geostationary satellites. In this study, three different products are used that employ such a blended precipitation scheme. All three data sets agree in their spatial resolution ($0.25^\circ \times 0.25^\circ$) and provide data in 3-hourly time steps, i.e. 12:00 UTC covering the period 22:30 to 01:30 UTC and so on. They are briefly described below.

The Tropical Rainfall Measuring Mission (TRMM) Multi-satellite Precipitation Analysis (TMPA) 3B42 Version 7 data set (Huffman et al., 2007) combines observations made by the TRMM satellite with other satellite systems, as well as land surface precipitation gauge analyses when possible. The passive microwave data, which has a strong physical relationship to the hydrometeors that result in surface precipitation, are collected from the Microwave Imager (TMI) on TRMM, Special Sensor Microwave Imager (SSM/I) on Defense Meteorological Satellite Program (DMSP) satellites, Advanced Microwave Scanning Radiometer – Earth Observing System (AMSR-E) on Aqua, and the Advanced Microwave Sounding Unit-B (AMSU-B) on the National Oceanic and Atmospheric Administration (NOAA) satellite series. The IR data, for the TMPA are collected by the international constellation of geosynchronous satellites. Additionally, data from TMI and the precipitation radar (PR) on TRMM are used as a source of calibration. The whole TMPA algorithm is constructed in four steps: (i) microwave precipitation estimates are calibrated and merged. (ii) IR precipitation data are produced using the calibrated microwave results. (iii) Then, the microwave and IR precipitation estimates are combined filling missing data. (iv) Lastly, rain gauge data are incorporated for the final product. For a detailed explanation of the TMPA algorithm see Huffman et al. (2007).

A similar approach is used for the CMORPH product (CPC MORPHing technique; Joyce et al., 2004), which uses passive microwave information from SSM/I, AMSU-B, AMSR-E and TMI. The main difference to TMPA is that data gaps are treated differently by transporting rainfall features via spatial propagation information, which is obtained from geostationary satellite IR data (Joyce et al., 2004).

PERSIANN (Precipitation Estimation from Remotely Sensed Information using Artificial Neural Networks; Sorooshian et al., 2000) assimilates IR precipitation estimates from geosynchronous satellites. These estimates are then calibrated using microwave precipitation from low Earth orbit satellites. It differs from the other above-described precipitation algorithms as its calibration technique involves an adaptive training algorithm that updates the retrieval parameters when microwave observations of precipitation become available (Sorooshian et al., 2000).

Inter-comparison studies show good agreement with ground-based precipitation observations for these data prod-

ucts (e.g. Ebert et al., 2007; Novella and Thiaw, 2010; Romilly and Gebremichael, 2011; Liu et al., 2015; Pipunic et al., 2013; Pfeifroth et al., 2016, and references therein), which is, however, variable for different geographic regions, surface types and rain intensities.

In our study, we apply each precipitation product individually to differentiate between days with or without rain fall. From the comparison of the corresponding results we find that the uncertainties and differences among the precipitation data sets have only minor effects on the obtained results (see Appendices A, E).

2.4 Soil moisture

The processes of nitrification and denitrification, which govern sNO_x fluxes, are closely related to the soil water content (Meixner and Yang, 2006). In situ measurements of soil moisture are sparse and difficult to extrapolate to broad geographic regions due to their highly heterogeneous nature. Combined satellite measurements of soil moisture overcome this issue by providing global coverage on a daily basis. Although the absolute value of soil moisture from merged satellite products has large uncertainties, relative variations triggered by precipitation events, should be evident in the time series.

Here, we use data from the ESA Soil Moisture CCI (Climate Change Initiative) ECV project, which merges level 2 soil moisture data derived from multiple satellite sensor products (Wagner et al., 2012) in order to construct a consistent long-time data set. Among the list of sensors that are included, are the C-band scatterometers on board of the ERS and METOP satellites and the multi-frequency radiometers SMMR, SSM/I, TMI, AMSR-E, and Windsat. The data sources include active (scatterometer) and passive (radiometer) microwave observations acquired preferentially in the low-frequency microwave range.

2.5 Other data sets

The data sets described above provide the basic information used in our research study. To evaluate and understand other influences on the retrieved trace gas levels; however, further atmospheric and environmental parameters are considered.

2.5.1 Lightning NO_x

Lightning represents a natural source of NO_x in the upper troposphere, especially in the tropics (Bond et al., 2002) and, thus, has a potential impact on the measured NO₂ slant column densities. Estimates of lightning activity are captured by satellite instruments as well as ground-based stations like the World Wide Lightning Location Network (WWLLN; Lay et al., 2004; Rodger et al., 2006). WWLLN offers a continuous data set, which is based on 20–30 ground-based sensors that detect impulsive signals from lightning discharges, *sferics*, in the very low frequency (VLF) band (3–30 kHz) (Dow-

den et al., 2002). This algorithm is, thus, more sensitive to cloud-to-ground flashes because of their stronger radiation in the VLF band compared to intra-cloud flashes. In order to be classified as a lightning event the lightning strike must be detected by at least five stations. The detection efficiency (DE) varies to a large extent due to the spatial distribution of contributing stations. For example, over Australia the DE is $\approx 80\text{--}90\%$, but only $\approx 10\text{--}20\%$ over Africa (Rodger et al., 2006).

2.5.2 Fire activity

Biomass burning in specific regions is a major source of trace gases and aerosol particles (Crutzen and Andreae, 1990) and, therefore, must be considered in our analysis. The MODIS global monthly fire location product MCD14ML (Giglio et al., 2006) is used to filter out locations affected by fires.

2.5.3 Meteorology

In order to understand the prevailing meteorology and filter for special circumstances in the Sahel region, modelled data of soil and air temperature, pressure, humidity as well as wind fields are taken from the ECMWF ERA-Interim analysis (Dee et al., 2011). The model data are acquired at a spatial resolution of 0.25° and a temporal resolution of 6 h over the period from 2007 to 2010. The data are publicly available via <http://apps.ecmwf.int/datasets/>.

2.5.4 Land cover

The analysis of trace gas time series is also split up for different land cover types as they are related to different soil compositions and, thus, different sNO_x potentials. Here, a land cover map for the year 2009 from the ESA initiated GlobCover project is used, which utilizes observations from the MERIS sensor on board the ENVISAT satellite mission with a spatial resolution of 300 m. The product is publicly available via http://due.esrin.esa.int/page_globcover.php and comprises 22 land cover classes defined with the United Nations (UN) Land Cover Classification System (LCCS) with an overall accuracy across all classes of 58 % (Arino et al., 2007; Bontemps et al., 2011). The data are downscaled using a most-common-value approach to identify dominant land cover types and to match the resolution of the other data sets. Thus, misclassifications might occur particularly over heterogeneous terrain and transition zones, while classification over homogeneous terrain is expected to be robust.

2.5.5 Water vapour

Total column observations of H₂O VCDs from GOME-2 give insight into the absolute humidity of the atmosphere at the time of the NO₂ observation from GOME-2 and, thus, a temporally more reliable estimate compared to modelled ECMWF data. H₂O VCDs from GOME-2 are derived based

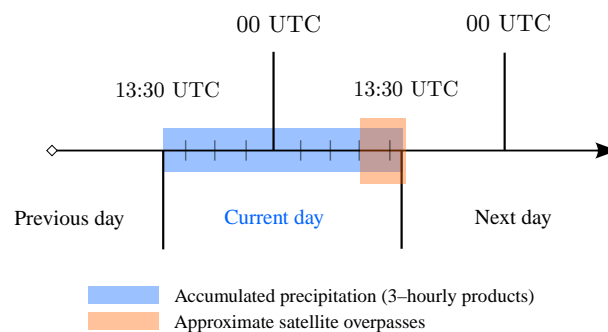


Figure 1. Schematic of the 24 h time period selected for the integration of precipitation data. The eight 3-hourly precipitation rates prior to the overpass times of the SCIAMACHY, GOME-2 and OMI satellite sensors are summed.

on a DOAS retrieval using a H₂O absorption band around 650 nm. Remaining non-linearities due to saturation effects are accounted for by a simple correction function determined from a radiative transfer model (RTM). Empirical AMFs are derived from the simultaneously measured O₂ absorption. Retrieval details and validation of the H₂O VCDs can be found in Wagner et al. (2003, 2006) and Grossi et al. (2015).

3 Methodology

A daily global time series data set spanning from 2007 to 2010 for grid boxes of $0.25^\circ \times 0.25^\circ$ is established comprising total precipitation and trace gas measurements. Level 2 products of the trace gases are screened for observations with effective cloud fraction above 20 % and a solar zenith angle above 60° . Furthermore, observations coinciding with lightning or fire events on the same day and within the same grid box are filtered out.

The 3-hourly precipitation data are integrated over the 24 h period prior to the satellite overpasses of GOME-2, SCIAMACHY and OMI to collocate rainfall events and trace gas observations. For example, in the Sahel region, which is the main study region of this paper, the precipitation data are integrated from 13:30 UTC of the previous day to 13:30 UTC of the current day as this corresponds to the local overpass time of OMI. This 24 h period is called *Day* in the following pages (see Fig. 1). For the global analysis, the temporal integration is shifted by 3 h in steps of 45° longitude.

As the highest soil emissions are expected at the start of a wet season after a long drought phase of several weeks to months, the transition between dry and rainy seasons is the primary focus of this work. However, the length of drought phases are quite different for semi-arid areas in the world, varying from very long (several months in winter) in the Sahel to shorter periods (several weeks to months in summer) in south-western Africa. Our approach considers grid boxes that experienced only little precipitation per day, e.g. < 2 mm, over a minimum number of days, e.g. 60 days, and a reason-

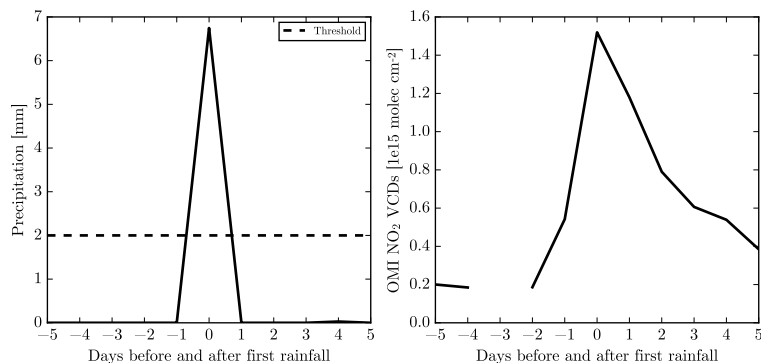


Figure 2. Time series of TMPA precipitation (a) and OMI NO₂ VCDs (b) for a 10 day period around the first rain event for a single grid pixel in the Sahel on 11 April 2008 at 15.25° N, 25.5° E. A threshold of 2 mm precipitation per day is chosen and at least 60 days of drought are required.

able amount of precipitation on the first rain day (> 2 mm). Then, the trace gas column densities around this *first day of rainfall*, which is counted as *Day 0* hereafter, are compared to the background levels during the preceding dry spell. The results vary slightly for different thresholds of the precipitation trigger, as shown in Appendix C. These sensitivity tests also show that a threshold of 2 mm day^{-1} leads to good statistics as well as representative responses in NO₂ VCDs.

Figure 2 depicts a typical time series of precipitation (left panel) and NO₂ VCDs (right panel) for a 5-day period around the first rain event (on Day 0) after a dry spell for a single grid pixel in the Sahel in April 2008. In the following, the days around the first day of rainfall are referred to as Day -3 , Day -2 , Day -1 , Day 0, Day $+1$, Day $+2$, Day $+3$ and so forth. It should be noted that there are almost no gaps in the precipitation time series; however, there are many in the trace gas time series. This is primarily due to the lower spatio-temporal coverage of trace gas products as well as the cloud, lightning and fire screening. In the example shown in Fig. 2 a $0.25^\circ \times 0.25^\circ$ pixel is chosen, which provides a complete NO₂ time series over 10 days. There is very little precipitation per day before the initial rain event. On Day 0, precipitation exceeds a threshold of 2 mm, used to differentiate between “rain” and “no rain”. Investigating the time series of NO₂ around the first day of rainfall reveals a strong enhancement on Day 0 and some smaller enhancement on Day -1 and Day $+1$, whereas from Day -10 to Day -2 the NO₂ VCD is close to the pre-event level; i.e. the average NO₂ VCDs of Day -5 to Day -1 . NO₂ VCDs after Day $+1$ stay systematically higher than the background.

The time series for this single grid box represents the evolution of precipitation and trace gas VCDs around the first day of rainfall for a single grid pixel (experiencing first precipitation after an extended drought) demonstrating the basic principle of this study.

In order to achieve representative results with improved statistics, averaging the time series over many pixels is necessary. However, as we focus on pulsed soil emissions, av-

eraging of time series from different pixels with rain events shifted in time has to be avoided. Furthermore, only a small subset of all possible pixels and their corresponding time series fulfils the conditions of the precipitation trigger. Thus, the individual time series are first synchronized in time relative to the first day of rainfall (Day 0). The subsequent averaging method is applied, in the following section, either with focus on high spatial resolution or with focus on best statistics at the expense of losing spatial resolution by averaging over larger areas.

In the following sections a drought period of at least 60 days followed by a rain event (precipitation > 2 mm) is referred to as the reference case. The drought period of about 2 months is chosen as we find the highest response in NO₂ with this setting. In Appendix B, the impact of drought lengths on the derived soil emission pulses is investigated.

4 Results

4.1 Global analysis

The algorithm described above, is applied to the full spatial extent covered by the TRMM/TMPA precipitation data set (-180 to 180° longitude, 50 to -50° latitude).

Figure 3a displays the number of valid OMI observations on $1.25^\circ \times 1.25^\circ$ grid pixels that fulfil the selection criteria, i.e. 60 days of drought and at least 2 mm of precipitation on Day 0. For most regions in the world enough data points are found for our analysis; exceptions are regions with no pronounced seasonality in rainfall (e.g. tropical rainforests, North America, Europe) and regions where rain occasionally falls during the dry season (Southeast Asia). Our algorithm is not optimized for those regions.

The days prior to the first rain are assumed to represent a background level of NO₂. Figure 3b depicts a background NO₂ map from OMI measurements obtained by averaging VCDs of the Day -10 to -2 .

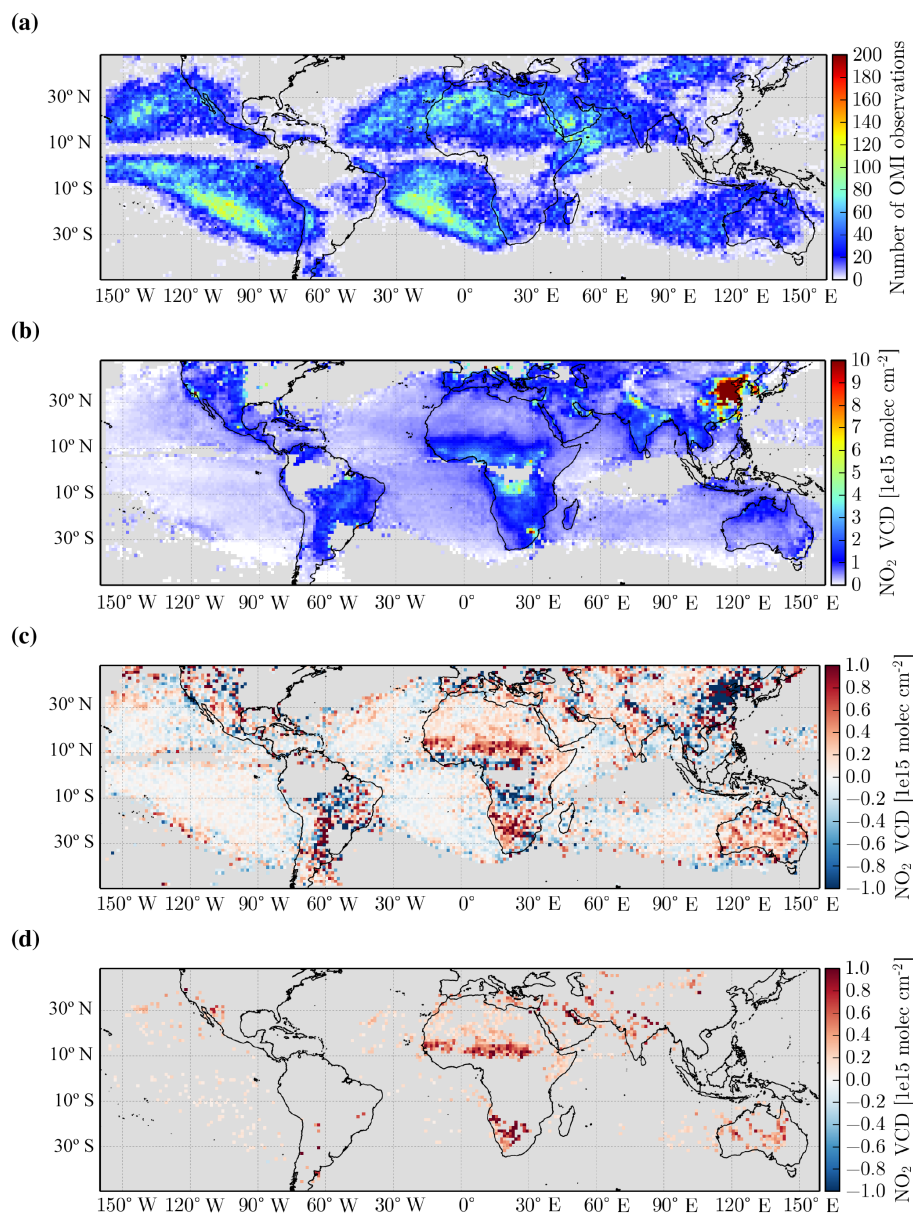


Figure 3. (a) Number of valid measurements per grid pixel on Day 0. (b) OMI NO₂ background levels averaged for days –10 to –2 before the first rain event after 60 days of drought for each pixel (0.25° lat/long) and then averaged for boxes of 1.25° lat/long. (c) OMI NO₂ VCD absolute differences on Day 0 (first day of rainfall) compared to Days –10 to –2. Reductions in NO₂ VCDs on Day 0 depicted in blue colours, enhancements in red. (d) as (c) but screened for significant changes (see text). Extensive enhancements over the Sahel and South Africa are evident. Pixels containing less than 20 measurements on Day 0 (or less than 50 measurements from Day –10 to Day –2) are screened out.

To examine variations in trace gas columns due to rain events, the enhancement of NO₂ VCDs on Day 0 are considered with respect to the background. Figure 3c shows the spatial distribution of these absolute differences for OMI. In Fig. 3d, data points within 2 times the standard deviation, σ , of the background variation in the respective grid cell are screened out. Furthermore, as the uncertainty from spatial representativeness becomes the dominant uncertainty contri-

bution if only few valid satellite pixels per grid cell are available (Boersma et al., 2016), at least 50 % of possible data are requested per grid pixel in order to be considered in this analysis. The corresponding results for NO₂ VCDs observed by GOME-2 and SCIAMACHY are similar to Fig. 3d, but are more affected by noise due to poorer statistics (see Appendix D).

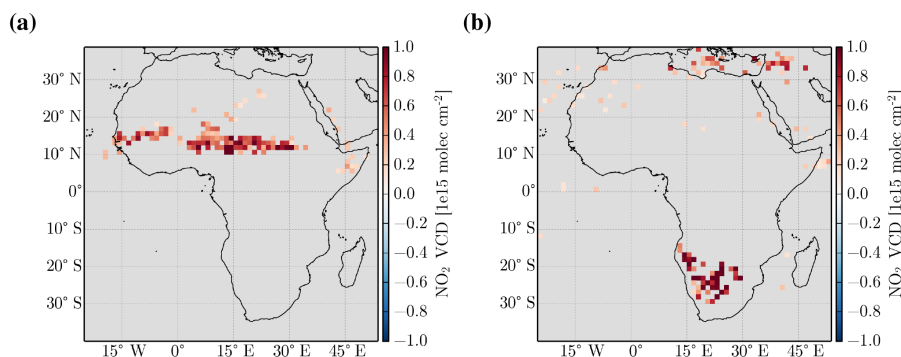


Figure 4. (a) Significant OMI NO₂ VCD enhancements (in 1×10^{15} molec cm⁻²) on Day 0 compared to the background level for April–May–June (2007–2010), which represents the start of the wet season after the dry period in the northern part of Africa. Extensive enhancements in NO₂ over the narrow band of the Sahel can be seen. (b) The same for September–October–November (2007–2010), whereby strong enhancements are found in south-western Africa. This time period reflects the transition time between the dry and wet season in this region.

The most eminent features are the high enhancements of OMI NO₂ column densities on Day 0 in the distinct band of the Sahel region around 15° N. Single grid pixels in this distinct band exceed absolute enhancements of 1×10^{15} molec cm⁻² over background.

Similar enhancements in the Sahel were also observed by Hudman et al. (2012). In the south-western part of Africa as well as over Australia spatially coherent enhancements are also present. Small-scale, local enhancements are found also, e.g. over India (also investigated by Ghude et al., 2010), regions nearby the Caspian Sea, the Middle East or China. An important finding is that there are no clustered reductions in NO₂ VCDs on Day 0. Since we do not apply any land–sea mask, oceans serve as control regions for our algorithm: no significant differences in NO₂ are found over the vast majority of oceans area. However, over the Mediterranean sea and in proximity to coastal regions over oceans, small-scale enhancements in NO₂ VCDs are detectable, which might be related to advection.

The applied algorithm considers all data regardless of the season. Analysing the data based on different periods of the year reveals local enhancements in NO₂ VCDs in semi-arid areas matching dry-to-wet season transitions in these geographic regions (Fig. 4). In April–May–June, Fig. 4a, the narrow band of the Sahel again is characterized by a mean enhancement of NO₂ of $\sim 1 \times 10^{15}$ molec cm⁻². This time period corresponds to the start of the rainy season in the Sahel after a long dry spell of 3–4 months. In September–October–November, Fig. 4b, the strongest peaks in NO₂ VCDs are observed in south-western Africa representing the start of the local wet season.

4.2 Detailed analyses over the Sahel region

The Sahel region represents a transition zone between the savannah in the south and the Saharan desert in the north. It is characterized by a strong seasonality in rainfall governed by

the north–south movement of the inter-tropical convergence zone (ITCZ). The northward movement of the ITCZ starts in March and the northernmost position is reached, at 15° N, in August. In the following four months the Sahel region receives about 90 % of its mean annual precipitation (Bell et al., 2000). The subsequent dry season begins in October and ends gradually with the start of the next wet season in April/May/June (AMJ period).

Previous studies (e.g. Jaeglé et al., 2004; Hudman et al., 2012) argue that in this distinct geographic band pulsed soil emissions of NO_x, which can be detected from space, occur at the beginning of the wet season in spring. Our findings support these previous studies and delineate this narrow band from 10 to 18° N and from the west coast of Africa essentially spanning the whole width of the continent, as shown in Fig. 4a. The pronounced sNO_x features in the band of the Sahel during the AMJ period enable a more detailed investigation of pulsed soil emissions.

We restrict our detailed analysis to the central and eastern part of the Sahel region (0–30° E, 12–18° N), similar to previous studies (i.e. Jaeglé et al., 2004; Hudman et al., 2012). The western part of the Sahel shows a slightly weaker NO₂ response to rain pulses, which might be related to different inter-annual variability patterns and seasonal cycles of precipitation regimes (Lebel and Ali, 2009).

In order to depict the general behaviour of trace gas responses and to improve the statistics, 4 years (2007–2010) of the AMJ period are averaged for the eastern part of the Sahel. Figure 5 depicts the evolution of multiple environmental variables around Day 0 averaged over the study region. The precipitation amounts from the three different products, indicated in grey shades in each panel of Fig. 5, generally agree in their relative variation, showing little rain before Day 0, a heavy rain event on Day 0 and slightly higher precipitation after the first rainfall event compared to Day –10 to Day –1. The discrepancies among TMPA, CMORPH and PERSIANN products indicate that some rain events might be

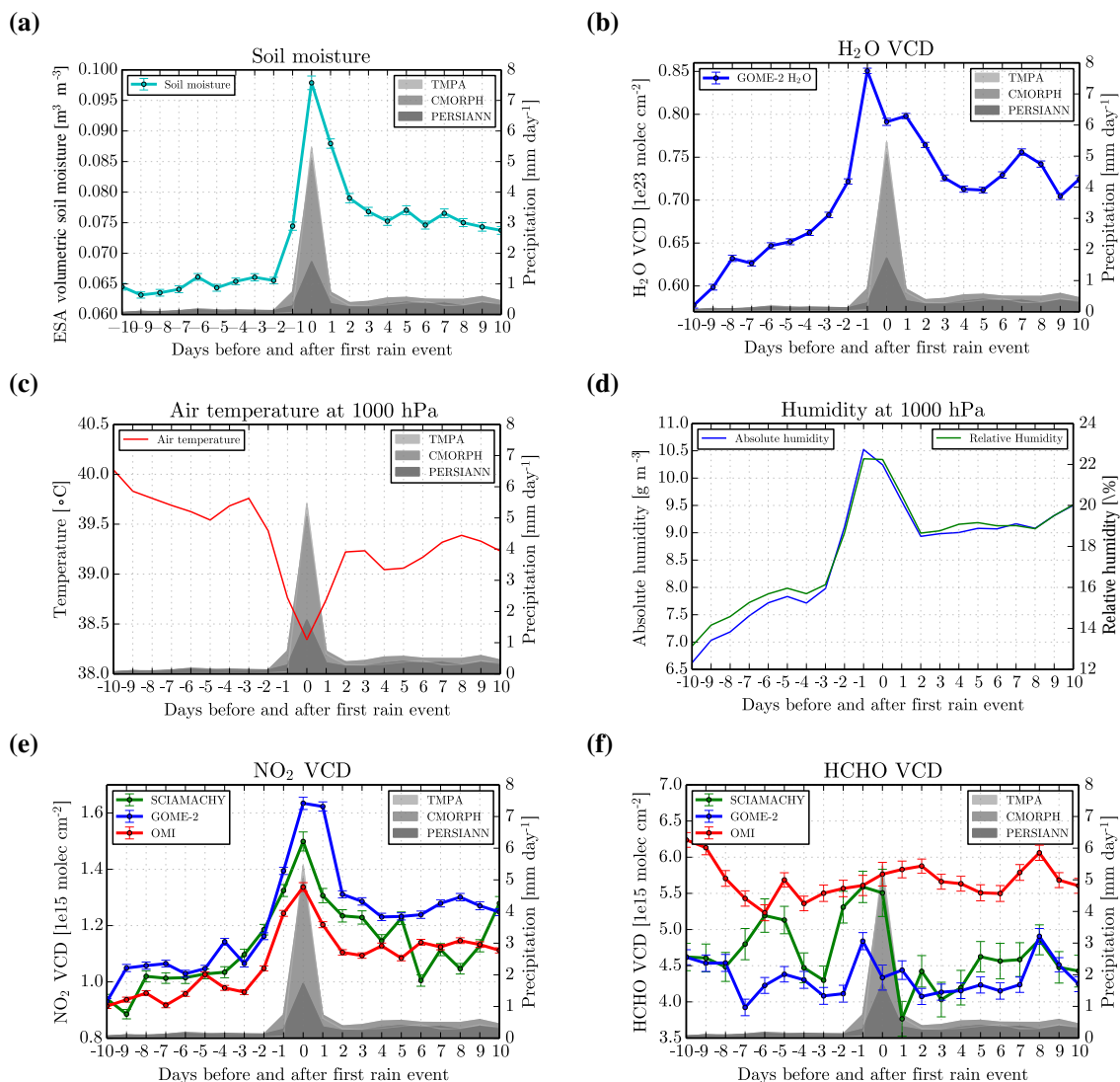


Figure 5. Temporal evolution of several quantities around the day with the first rain event for the Sahel region after at least 60 days of drought for April/May/June (2007–2010). Grey shaded areas represent precipitation estimates from TMPA, CMORPH and PERSIANN. (a) Blended ESA CCI soil moisture. (b) Water vapour total column densities from GOME-2. (c) Temperature at 1000 hPa from ECMWF Interim Analysis. (d) Relative and absolute humidity at 1000 hPa from ECMWF Interim Analysis. (e) NO_2 VCDs from SCIAMACHY, GOME-2 and OMI with standard mean error (SME). (f) HCHO VCDs from SCIAMACHY, GOME-2 and OMI with SME.

missed or assessed differently by the individual data products. Nevertheless, considering CMORPH or PERSIANN data as trigger leads to comparable responses in trace gases around the first day of rainfall (Appendix A).

The immediate wetting of the dry surface on Day 0 is captured well by satellite observations of the volumetric soil moisture content as seen in Fig. 5a. After the initial wetting of the soil, the moisture content drops quickly during the following 3 days due to infiltration and evaporation. Similar behaviour is observed for total column densities of water vapour from GOME-2 in Fig. 5b. Water vapour content in the atmosphere gives insight into the ambient humidity and may indicate impending rain events, as humidity in the at-

mosphere typically rises prior to precipitation. On Days –10 to –2 water vapour steadily builds up in the atmosphere and peaks 1 day before the initial rain event. On Day 0 and the following 3 days, the water vapour column densities drop, which is probably caused by, on the one hand, the removal of atmospheric water by precipitation and and, on the other hand, by transport of dry air masses over the study area. The results for NO_2 VCDs using the three satellite instruments (OMI, GOME-2 and SCIAMACHY) show a consistent enhancement around the first day of rainfall (Fig. 5e). This points to a strong source linked to the dry–wet transition, i.e. the precipitation trigger. However, the magnitude of the enhancement varies for the three instruments. The standard error of

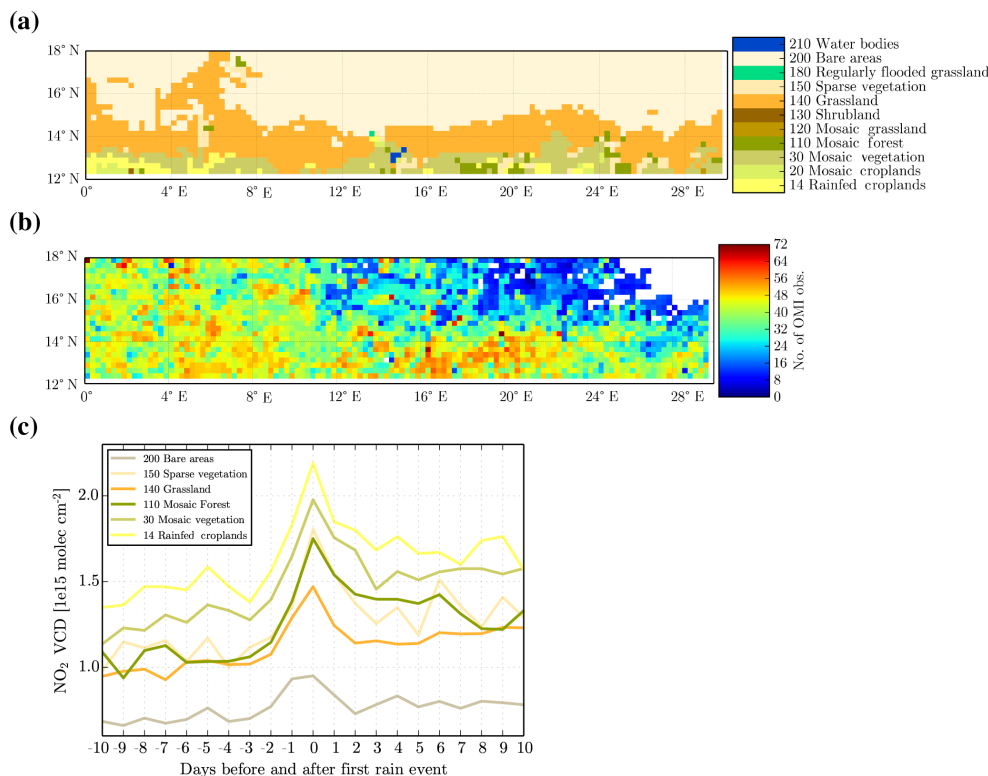


Figure 6. (a) ESA GLOBCOVER land cover classification for the Sahel downscaled to $0.25^\circ \times 0.25^\circ$ resolution with the corresponding (official) identification number, short name and colour information for each class. (b) Spatial location and number of OMI observations for the reference case analysis (AMJ, 2007–2010). (c) Rain-triggered NO₂ enhancements from OMI for the Sahel region separated by the dominant land cover types.

the mean (SME) value is indicated for each instrument and is generally smaller for OMI, which has the best statistics.

The average absolute enhancement in the Sahel for GOME-2 NO₂ on Day 0 compared to the background levels is about 5×10^{14} molec cm⁻², whereas OMI and SCIAMACHY only observe an absolute enhancement of ~ 3 and 4×10^{14} molec cm⁻², respectively.

The different magnitudes of the enhancements cannot be solely explained by differences in overpass time or pixel size as GOME-2 and SCIAMACHY are similar in both aspects. Furthermore, higher emissions are expected in the afternoon, i.e. at OMI overpass time, when the temperature is higher. The corresponding SCDs, however, (see Fig. 9e) indicate that the differences seen in the NO₂ VCDs are mainly caused by differences in the AMF calculation for the three data products.

Note that the enhancement is about 5×10^{14} molec cm⁻² on average, while it was shown in the previous section that for single 1.25° boxes the absolute enhancements can be as high as $\sim 1 \times 10^{15}$ molec cm⁻². Smaller grid pixels show enhancements of up to $\sim 4 \times 10^{15}$ molec cm⁻², and for single events even larger enhancements are found.

Another striking feature, similar to the results for soil moisture, water vapour and precipitation, is the generally

higher NO₂ VCDs during the 10 days following the first rain-fall event compared to the background levels before Day 0. In Sect. 4.4 and 4.5, this important finding is studied more in detail by analyzing the NO₂ levels after Day 0 depending on wind conditions and the precipitation on Day +1 and beyond.

As indicated in the introduction chapter, HCHO emissions from soils were found in several laboratory and field experiments (e.g. Veres et al., 2014). In Fig. 5f we also analysed HCHO VCDs from OMI, SCIAMACHY and GOME-2 for potential pulsed emissions triggered by precipitation. The time series of HCHO for the three instruments, however, show no significant enhancement around the day of the first rain event. Possible reasons are the low signal-to-noise ratio for HCHO observations or very low emission rates.

4.3 Land cover analysis

Soils from different regions and land types are differently affected by precipitation and vary strongly in their microbial composition, nitrogen availability and pH values, which presumably leads to strong differences in emission fluxes from soils. In the following study, the ESA GLOBCOVER land cover classification is used to characterize different land cover types. The data set is scaled down from the initial

300 m resolution to the $0.25^\circ \times 0.25^\circ$ grid using a most-common-value method. The resulting land cover map is shown in Fig. 6a.

For different land cover types, both the NO₂ response on Day 0 and the background level of NO₂ vary systematically, see Fig. 6c. The observed NO₂ background VCDs per land cover type in the Sahel are mainly governed by biogenic emissions from soils and biomass burning. Anthropogenic activity and related emissions such as domestic fires or fertilized fields are at a very low level, and originate mostly from the southern, more populated part of the Sahel (Delon et al., 2010).

Systematic variations among the different land cover types are captured well: barren land, for example, shows the lowest levels of NO₂ compared to all other land cover types. Barren land relates to deserts with very low nitrogen input resulting in low sNO_x, even after wetting. This land type is also associated with fewer rainfall events, see Fig. 6b. Mosaic land covers (a mixture between various vegetation types, grassland, cropland or forest), refer in this area to the loose term *savannah* delineating the transition zone between tropical forests and deserts. Savannahs can comprise various land cover subtypes and are characterized by distinct dry and wet periods with strong vegetation density and productivity during the wet season in summer. It is expected that savannah and cultivated land used for agriculture show strongest responses to initial rain events due to their higher potential for soil emissions. Figure 6c confirms these hypotheses: the largest NO₂ enhancements are found for cropland and savannah; grassland shows a significant, but smaller response; and the driest land cover type (bare area) shows only slightly enhanced NO₂ on Day 0.

4.4 Influence from other sources on the NO₂ signal

In this section, we investigate the effects of possible additional sources of NO_x such as fire or lightning and systematic errors in the satellite retrieval due to, e.g., changes in cloud fraction. To minimize the influence of these effects, our algorithm excludes measurements where lightning, fires or an effective cloud fraction > 20% are detected.

4.4.1 Lightning NO_x

Lightning is a natural source of NO₂ in the upper troposphere (e.g. Schumann and Huntrieser, 2007, and references therein). Since lightning typically occurs in high convective clouds that may correlate with the first rain event, our analysis is potentially affected.

Figure 7 depicts daily time series for NO₂ VCDs, precipitation and lightning counts averaged for the years 2007 to 2010. The seasonal evolution of the number of lightning strikes closely follows the precipitation patterns. Figure 7 also illustrates that lightning is not a governing source of NO_x in the Sahel as no correlation between lightning strikes

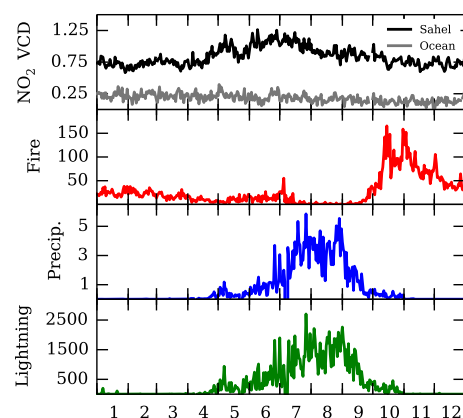


Figure 7. Daily time series for the Sahel region ($0\text{--}30^\circ$ W, $12\text{--}18^\circ$ N) averaged for the years 2007, 2008, 2009 and 2010. The first row of each panel shows mean NO₂ VCDs from OMI in molecules cm^{-2} (black) and a clean ocean reference (grey, $130\text{--}150^\circ$ W, $12\text{--}18^\circ$ N). The second row shows the number of active fire counts in the Sahel from MODIS. The third row shows average precipitation from the TMPA/TRMM product in mm. The fourth row shows the number of lightning strikes detected by WWLLN.

and NO₂ VCDs can be found, although a direct proportionality would be expected. Precipitation also does not correlate well with the observed seasonal cycle in NO₂. This is, however, expected as microbial emissions of NO_x from soils are not a linear function of soil moisture content or precipitation.

Figure 8 shows results for the reference case, similar to Fig. 5, but with (solid lines) and without (dashed lines) lightning screening; i.e. grid pixels coinciding with a lightning event are removed. Because of the low DE of the WWLLN in African regions ($\sim 20\%$) the lightning screening is also tested for central Australia ($15\text{--}30^\circ$ W, $2\text{--}10^\circ$ S) where the DE of the WWLLN is very high ($80\text{--}90\%$). Turning off the lightning screening leads to very similar results as for the reference case, but with a slightly stronger response in NO₂ VCDs on Day 0 for all three instruments. While this enhancement might be partly caused by the additional NO_x produced by lightning, also a larger number of true precipitation-triggered events that lead to soil emissions may be included in this analysis. This is conceivable as clouds and thunderstorms accompanied by lightning strikes lead to the most heavy precipitation events. As the screening only causes minor changes in peak NO₂ columns, lightning can be excluded as the main cause of the observed NO₂ enhancements.

4.4.2 Fire

The seasonal cycle in fire counts, depicted in Fig. 7, shows the highest activity in the Sahel in October and November for the years 2007 to 2010, while average NO₂ VCDs are the highest in summer.

Switching off the routine data screening for pixels that coincide with fire events in the same $0.25^\circ \times 0.25^\circ$ grid pixel

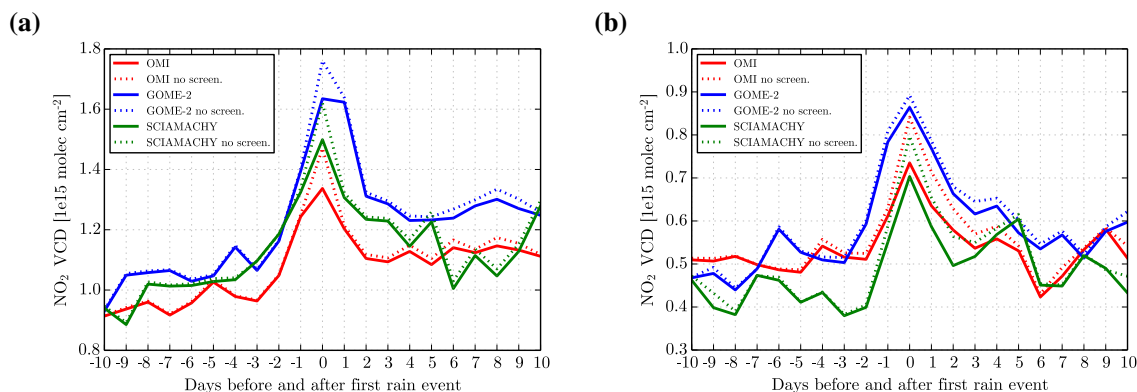


Figure 8. Effect of lightning screening on the response of NO₂ VCDs around the first day of rainfall after a prolonged dry spell. **(a)** NO₂ VCDs for the Sahel region from SCIAMACHY, GOME-2 and OMI without lightning screening (dashed lines) and with lightning screening (solid lines). **(b)** The corresponding results for central Australia (15–30° W, 2–10° S).

results in no change of the NO₂ signal (not shown). This is due to the fact that only very few fires occur in the wet season, on average only in 0.002 % of all individual time series on Day 0 in the reference case, excluding fire as an important NO₂ source within our analysis.

4.4.3 Cloud effects

We have investigated possible cloud effects on our results by analyzing the temporal evolution of the mean cloud fractions (CF), NO₂ VCDs and NO₂ SCDs around the precipitation event. The latter was added as it provides the actual measured signal without involving a tropospheric AMF, which is generally very sensitive to clouds.

Figure 9a depicts the mean effective CF for SCIAMACHY, GOME-2 and OMI for the Sahel region. The differences of the absolute value of the CF are probably related to the different cloud algorithms between GOME-2/SCIAMACHY (FRESCO+) and OMI (OMCLD02). The different temporal variation might also be partly related to the different overpass times and pixel sizes among the three satellite instruments. From these results we conclude that the observed NO₂ peaks around Day 0 are not caused by cloud effects for the following reasons: first, for all sensors only small cloud fractions (< 11 %) are found (for measurements with CF < 0.2). Second, for SCIAMACHY and GOME-2 observations no systematic temporal variation of the CF is found. Third, the small but systematic enhancement of the CF around Day 0 found in the OMI observations would rather lead to a decrease (due to the shielding effect) of the NO₂ SCDs around Day 0 as soil emissions are expected to remain close to the surface. If only measurements with cloud fractions > 20 % are considered, no spike is observed in the SCDs (Fig. 9f); GOME-2 and OMI even show a dip on Day 0, which is also seen in the respective VCDs (Fig. 9d). Interestingly, while there is a strong systematic enhancement of the FRESCO+ and OMCLD02 cloud fractions, the NO₂

SCDs show no peak around Day 0 for GOME-2 and OMI. This indicates that clouds effectively shield the pulsed soil emissions.

4.4.4 Influence of transport processes

Finally the possible influence of transport processes, which might be correlated with the occurrence of the first rain event, is investigated. As depicted in Fig. 10, a strong southerly wind is blowing at ground level (1000 hPa) the two days before the first rain event and on Day 0 in the Sahel. In order to investigate whether polluted air from southern locations, especially the tropics, is transported northward into the Sahel, we repeat the analysis for days governed by either northerly or southerly winds (Fig. 11). For the distinction between both directions we require that wind vectors from ECMWF at three different altitudes (600, 850 and 1000 hPa) point to the same direction in either case. The left panel in Fig. 11 depicts results for northerly winds; the right panel for southerly winds. Although the background levels of NO₂ are reduced on days with northerly winds, enhancements in VCDs around the first day of rainfall remain apparent despite low statistics, especially for OMI and GOME-2 observations. For days with southerly winds the background is slightly higher and clear spikes for the OMI and GOME-2 observations can also be detected. Hence, these findings indicate that atmospheric transport has a systematic influence on the background NO₂ levels (see also Sect. 4.5), but not substantially on the enhancement around Day 0.

4.5 Latitudinal background correction and emissions after Day 0

In the reference case analysis presented in the sections above, NO₂ VCDs show an enhancement with respect to the background, i.e. the average NO₂ VCDs before Day –1, not only on Day 0, but also on Day +1, Day +2 and Day +3. It is assumed that the *background* NO₂ VCDs are not influenced

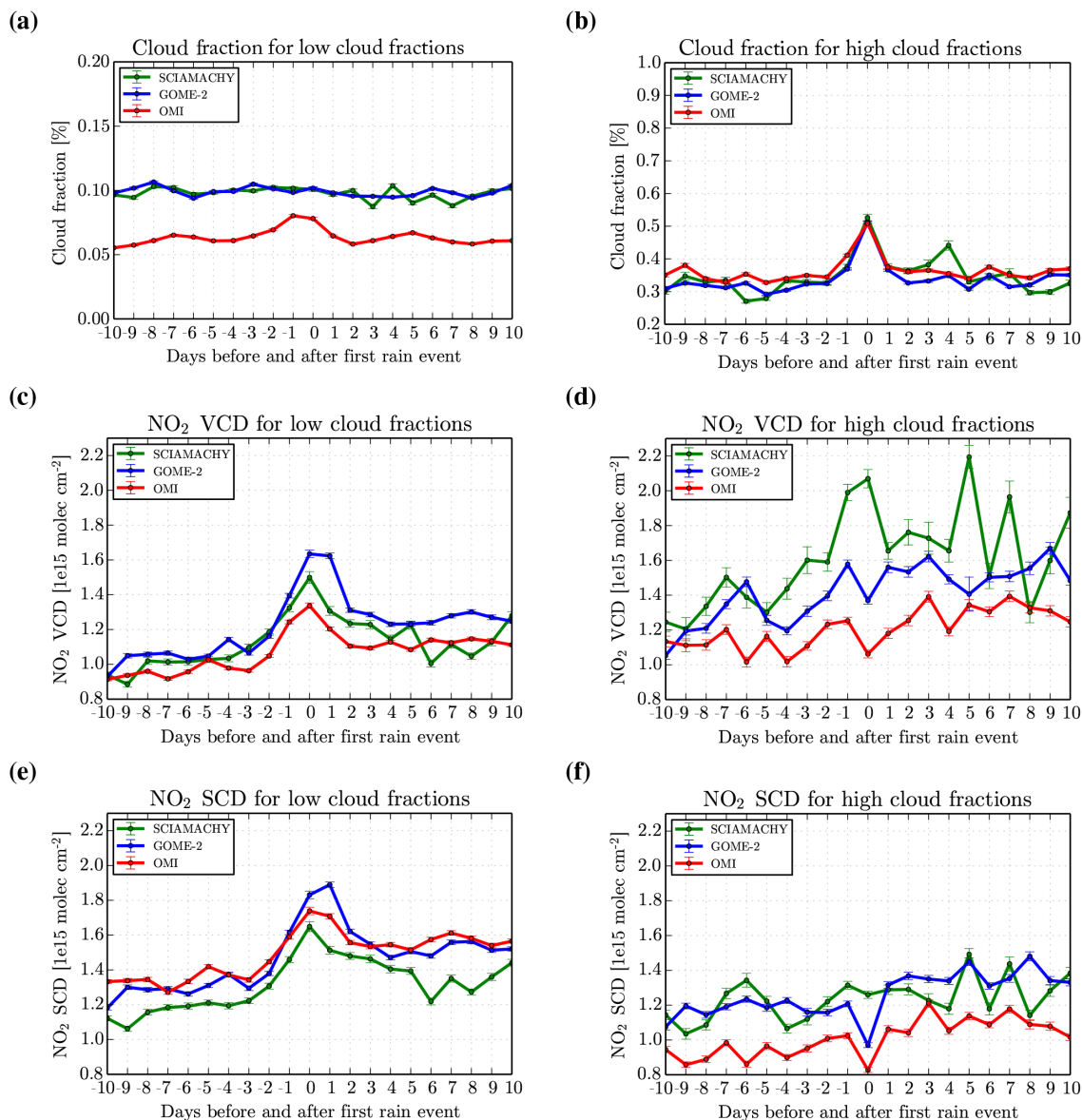


Figure 9. Investigation of cloud effects on the retrieved NO_2 SCDs and VCDs. **(a)** Mean cloud fraction of the three satellite instruments for the reference case (cloud fraction < 20 %). **(b)** Mean cloud fraction of the three satellite instruments but considering only observations with cloud fraction > 20 %. **(c)** NO_2 VCDs for the reference case. **(d)** NO_2 VCDs only considering observations with high cloud cover (cloud fraction > 20 %). **(e)** NO_2 SCDs for the reference case. **(f)** NO_2 SCDs only considering observations with high cloud cover (cloud fraction > 20 %).

by the precipitation-triggered sNO_x pulsing event and, thus, can be used as reference to derive an absolute enhancement in NO_2 VCDs predominantly induced by pulsed soil emissions. However, it is shown in Figs. 5e and 9c, e that the NO_2 VCDs after the pulsing event (Day +3 to Day +10) are consistently higher compared to the background before Day 0. This could be related to inflow of soil NO_x from adjacent pixels, which receive the first rain shortly after. However, initial tests showed that the number of such incidents is quite small (less than 5 %). For this reason, and because the effect is pos-

sibly offset by sNO_x advection out of the pixel of interest, it is assumed that the effect of inflow is not dominant. As we focus on events with strong emissions (compared to background), a “smearing effect” by advection leads to a consistent underestimation of the peak and subsequent emissions. Thus, we conclude that inflow cannot explain the enhancement for 14 days after the first rain event. Furthermore, it remains unclear to what extent the enhanced NO_2 VCDs are affected by a possible underlying change in the background.

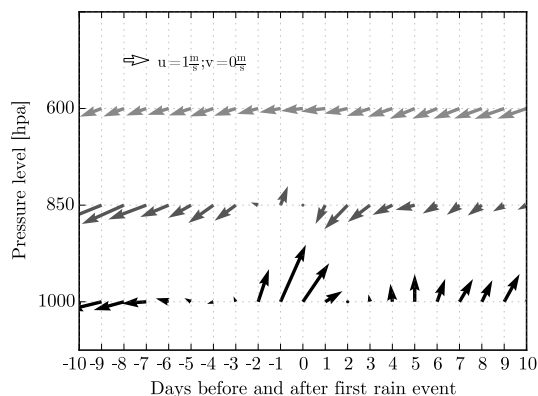


Figure 10. Mean ECMWF wind vectors at three different pressure levels. At the surface, a strong south-westerly wind is blowing the 2 days before the first rain event in the Sahel region followed by northerly winds. At 600 hPa winds are constantly from the northwest.

This leads to four interesting questions. (i) Are the slightly enhanced NO₂ VCDs after Day 0 related to the pulse on Day 0? (ii) In case the enhanced NO₂ VCDs after Day 0 are (partly) caused by other sources, what effect does a background correction have on the retrieved absolute enhancements in NO₂ VCDs around Day 0? (iii) Is continuous precipitation the cause for the enhancement after Day 0? (iv) In case the enhanced NO₂ VCDs after Day 0 are only related to the pulsed rain event, can we give quantitative estimates on these “continuous” soil emissions?

Figure 12a depicts the reference case analysis for the Sahel region with respect to 120 days around the first day of rainfall after the drought period. The NO₂ VCDs observed by the three satellite instruments show consistent patterns in the spike around Day 0 and still slightly enhanced NO₂ VCDs 60 days after Day 0.

To investigate whether the increased NO₂ VCDs after Day 0 are related to the pulsed rain on Day 0 or caused by a general change of the background NO₂ VCDs (e.g. related to a seasonal variation), we try to estimate the temporal evolution of the background (not affected by a pulsed rain event) in the following.

In a first attempt NO₂ VCDs are averaged over all grid pixels located at the same latitude as the identified rain events assuming latitudinal homogeneity in NO₂ background VCDs. This assumption is justified in the Sahel due to the latitudinal distribution of its land cover types governing NO₂ VCDs (the corresponding results are depicted in Fig. 12b). While compared to Fig. 12a, a much smoother temporal evolution is found (because more data are averaged), but apart from the much smaller spike on Day 0, very similar values can be seen in both panels. This confirms our assumption that the main part of the increase of the background value is not caused by the precipitation on Day 0. However, the spike in NO₂ VCDs around Day 0 is still evident because this averaging method

still considers the initial pixel with its adjacent neighbours, which are probably affected by either the overall precipitation pattern or spatial aliasing effects during the gridding of the NO₂ data products. Thus, in Fig. 12c a 10 pixel buffer is additionally applied to the algorithm. Screening out such pixels leads to a time series of NO₂ without the distinct spike around Day 0.

The time series of NO₂ VCDs retrieved using the two latitudinal averaging methods is denoted as the prevailing background and is subsequently subtracted from the reference case analysis (Fig. 12). In the first case, without the application of an additional buffer (Fig. 12d), absolute enhancements of 0.43×10^{15} molec cm⁻² for GOME-2 and SCIAMACHY are found on Day 0. Also a steady increase in NO₂ VCDs several days prior to Day 0 is observed. Although the pronounced spike in NO₂ VCDs decreases rapidly in the days following Day 0, it lasts several weeks until the VCDs reach a minimum (but stays still slightly higher than on Day -60 to Day -20). A similar behaviour is observed for the case study with buffer screening (Fig. 12e). Here, absolute enhancements of 0.4×10^{15} molec cm⁻² for OMI and 0.62×10^{15} molec cm⁻² for GOME-2 and SCIAMACHY are found on Day 0.

From these results we conclude that the slightly enhanced NO₂ VCDs after Day 0 are related to the precipitation on Day 0 at or close to the considered location. As our focus is on the quantification of the emission pulse triggered by the first rain of the wet season, it still needs to be clarified whether the enhanced NO₂ VCDs after Day 0 are induced by the initial precipitation on Day 0 or by continuous precipitation during the following days. To answer this question we extract time series with the additional selection criterion of 3, 5, 10 and 20 days of no precipitation following Day 0. Figure 13a depicts the OMI NO₂ VCDs for 0, 3, 5, 10 and 20 days without precipitation after Day 0. The intercomparison of these time series is not straightforward as the background values vary for each case indicating that the time series are captured at different dates throughout the April–May–June period. Longer drought periods after Day 0 are more likely at the very beginning of the wet season (April), whereas more constant rainfall dominates at a later stage, e.g. in June. In this time period background NO₂ VCDs generally increase in the Sahel. For this analysis we assume that the impact of the different dates only affects the background and not the enhancement on Day 0 as the selection criteria (precipitation and drought length thresholds) presumably have the largest effect. In order to analyse the enhancement around Day 0 only, we apply the above-described latitudinal background correction to each time series individually, which reduces the influence of the background drastically. Figure 13b,c show the corresponding background NO₂ VCDs derived without and with the aforementioned buffer screening applied. Naturally, the absolute change between the different background time series is smaller compared to Fig. 13a as they represent averages over all pixels on the

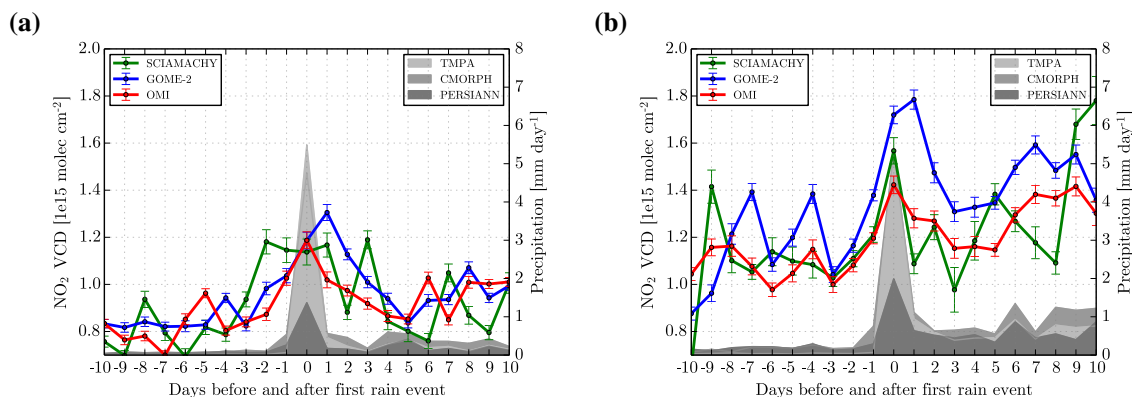


Figure 11. Same as Fig. 5d, but filtered for (a) northerly and (b) southerly winds. The filter criterion is fulfilled, if the wind direction at 600, 850 and 1000 hPa is north or south, respectively.

same latitude. The changes on Fig. 13c are even smaller because the pixels in proximity to the triggered rainy pixel are excluded from the averaging. Finally, Fig. 13d and e depict the differences between panel a and panels b and c, respectively. As expected, the enhancements in NO_2 VCDs around Day 0, are more pronounced for cases including a 10 pixel buffer during the background correction. Although the absolute enhancement on Day 0 is almost identical for the different cases, the time series still differ in the observed background NO_2 VCDs. These systematic differences, seen in Fig. 13d and e, hint at more complex variations in the background, which are not entirely resolved by our correction. They could also be related to the fact that for the cases with longer dry periods after Day 0 the probability of precipitation in the vicinity of the considered location is lower. This implies, again, also differences in space and time of the observations, which influences the observed NO_2 VCDs.

Generally, we find that the NO_2 VCDs stay enhanced after Day 0 for a period of about 2 weeks, almost independent from the duration of the dry period after Day 0. This gives rise to the assumption that the enhanced emissions are mostly caused by the initial rain event on Day 0. Here, only results for OMI are presented because it has best statistics. Nevertheless, the analysis with data from the other instruments leads to the same conclusion.

4.6 Further study regions

As could be seen in the global analysis in Fig. 3, large-scale hot-spots in NO_2 VCD enhancements are not only detectable in the Sahel, but also in south-western Africa and in Australia. Subsequently, we present also the average NO_2 VCDs around the first day of rainfall for all three satellite instruments in these two regions.

Figure 14a depicts the results for south-western Africa (17–23° E, 22–28° S) for a drought period (precipitation < 2 mm) of at least 60 days in the months September–October–November 2007–2010 representing the transition

phase between the dry summer and following wet season. Compared to the Sahel reference case, the evolution of NO_2 VCDs before and after the first day of rainfall increases and decreases more gradually without having a distinct spike on Day 0. This might be due to different environmental conditions such as soil type or lower statistics because of the much smaller spatial extent. It is, thus, more difficult to estimate the absolute enhancement compared to a defined background level. The difference between highest and lowest NO_2 VCDs in the full time series is $\sim 0.5 \times 10^{15}$ molec cm^{-2} for all three instruments.

Figure 14b shows the analysis results for NO_2 VCDs for the central part of Australia (120–145° E, 22–31° S) for the time series from 2007 to 2010. Since the seasonality in rainfall in this region is less pronounced, the full time series is considered in the analysis. The well pronounced spikes show an absolute enhancement of $\sim 0.3 \times 10^{15}$ molec cm^{-2} for the three instruments, which is comparable to the findings from the Sahel and south-western Africa.

5 Discussion

5.1 Estimated nitrogen emission fluxes from the emission pulse

Soil emissions of trace gases are not only limited to the specific days we investigated in this study (based on the selection criteria for the temporal evolution of precipitation), but can play an important role in the atmosphere during specific seasons and throughout the whole year (Steinkamp et al., 2009). Global chemistry models considered the mean seasonal behaviour of soil emissions in the past, but they were insensitive to rapid changes on a daily basis, e.g. during the onset of the wet season. Pulsed emissions of sNO_x have been recognized to be a significant short-term local enhancement, which can be parametrized in GCMs as shown by Hudman et al. (2012) for the GEOS-CHEM model. The latter study investigates

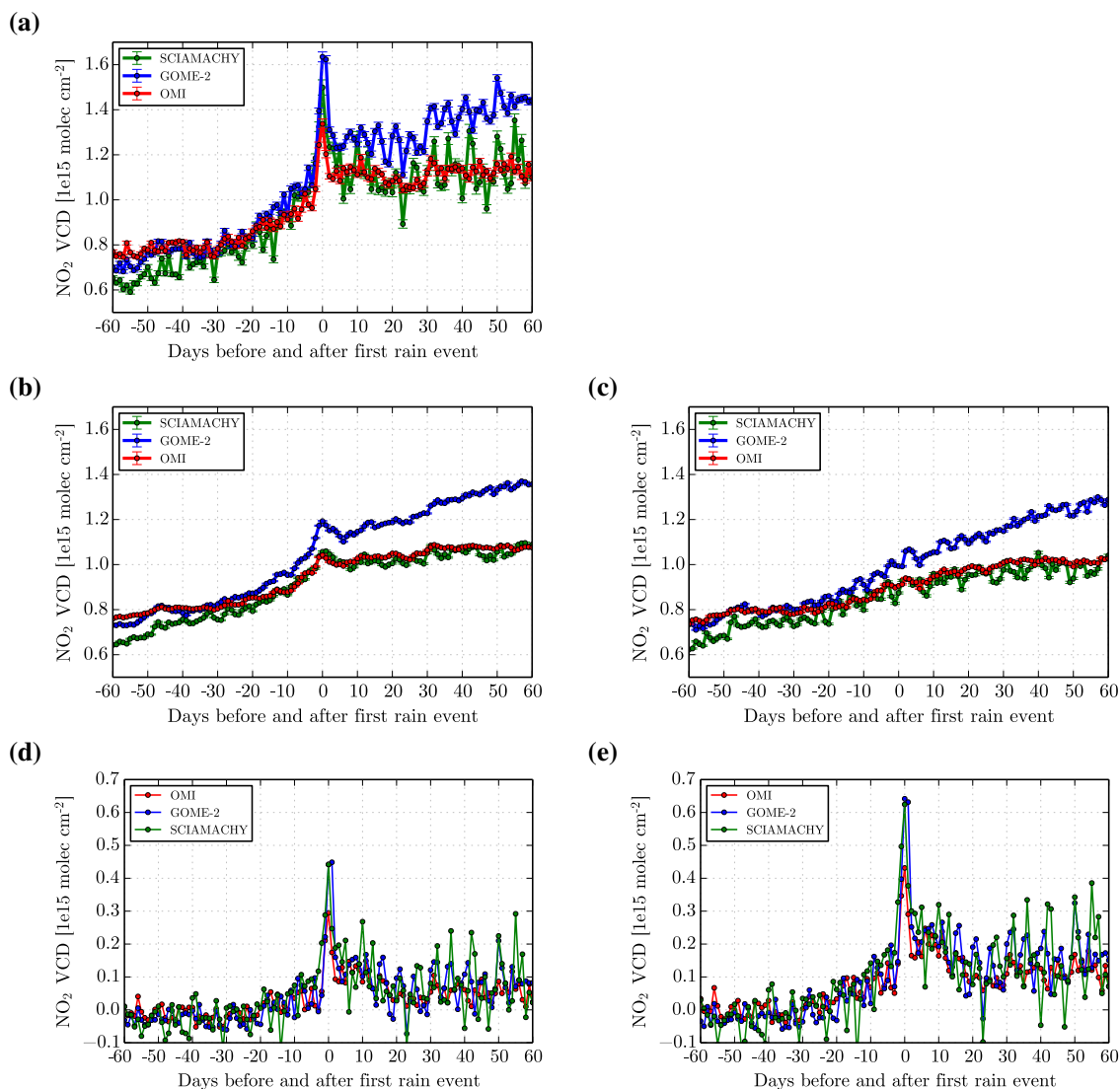


Figure 12. Analysis of NO₂ VCDs 60 days before and after the first day of rainfall in the April–May–June period for the Sahel region. (a) NO₂ VCDs from OMI, GOME-2 and SCIAMACHY. (b) Latitudinal averaged NO₂ VCDs corresponding to the reference (for details see text). (c) Latitudinal-averaged NO₂ VCDs corresponding to the reference considering an additional buffer of 10 pixels around the actual-triggered pixel to avoid influence of enhanced NO₂ VCDs in the vicinity of the precipitation events. (d) Background corrected NO₂ VCDs: (a–b). (e) Background (with buffer) corrected NO₂ VCDs: (a–c).

pulsed soil emissions of NO_x in the Sahel region and finds a comparable magnitude (49 % relative increase of OMI NO₂ VCDs on Day 0) and length of the pulsing event (1–2 days) following the first rainfall. Here, we provide further evidence supporting that and other reported studies, i.e. the observed enhancements in NO₂ VCDs are consistent for multiple instruments and are not introduced by retrieval errors or interfering sources.

For the Sahel region we find significant mean enhancements on the first day of rainfall in April–May–June averaged over four seasons (2007–2010) of $\sim 4 \times 10^{14}$ molec cm⁻², as observed by OMI, after the prolonged dry spell. However, we see much stronger enhancements for single pix-

els on the original fine resolution grid (0.25°) of up to $\sim 4 \times 10^{15}$ molec cm⁻². Considering these values as upper and lower limits for the sNO_x enhancement on Day 0, we can estimate emission fluxes. The top-down emission flux for NO_x can be inferred from the NO₂ VCD by mass balance: $E = \Omega_{\text{NO}_2} / \tau_{\text{NO}_2}$ with Ω_{NO_2} , being the tropospheric NO₂ VCD and τ_{NO_2} the lifetime. The lifetime for τ_{NO_2} is mostly determined by the oxidation of NO_x to HNO₃ in the boundary layer and typically ranges between 4 and 10 h in the tropics (Martin, 2003). Consequently, we find that the emission flux of nitrogen (N) for pulsing events, considering an assumed NO₂ life time of 4 h, in the Sahel is between 6 ng N m⁻² s⁻¹ for a conservative estimate and

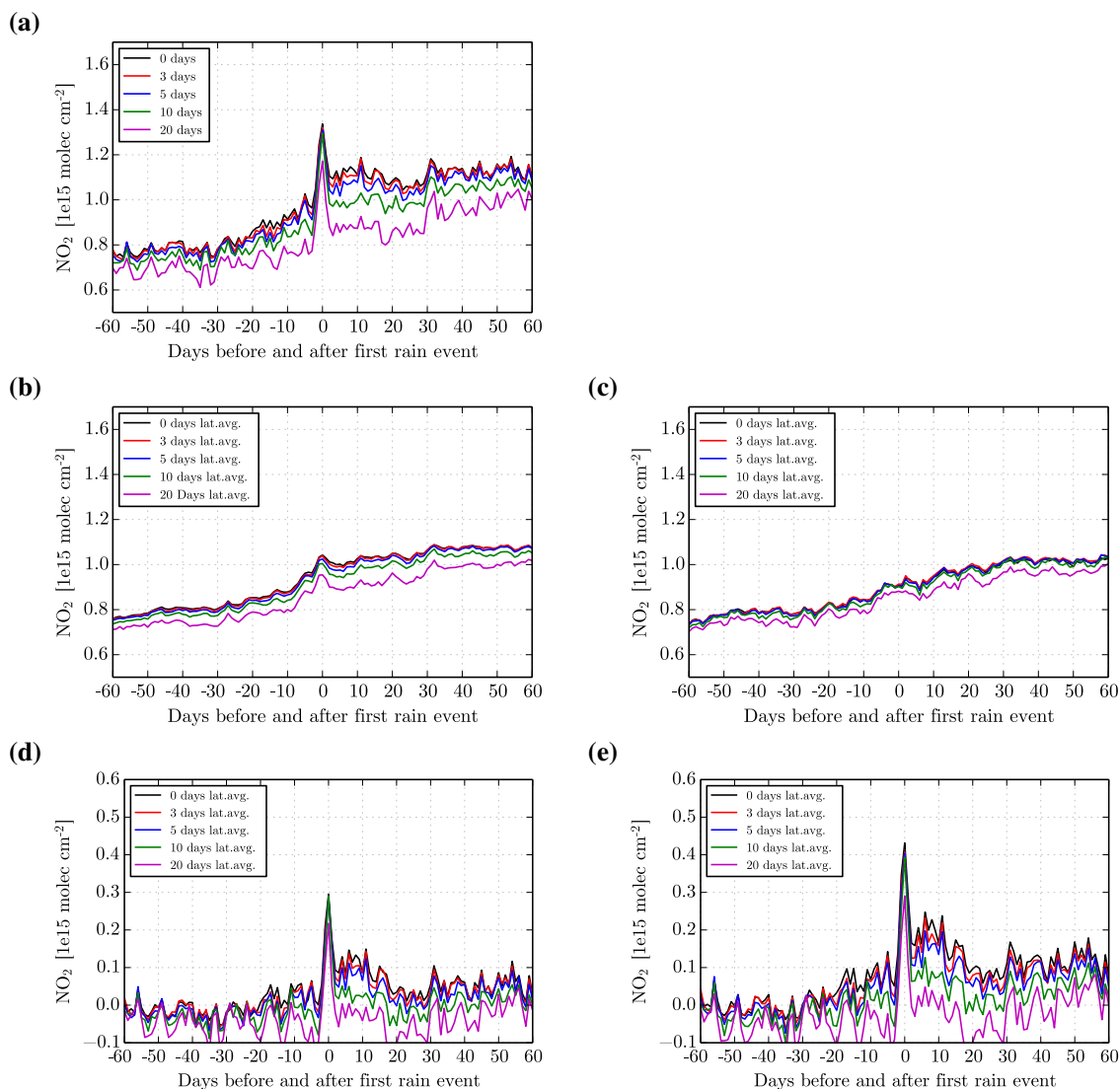


Figure 13. Investigation of the effect of different periods of dry days following Day 0. **(a)** Reference case analysis for OMI NO_2 VCDs filtered for time series experiencing 0, 3, 5, 10 and 20 days of drought after Day 0. **(b)** Background time series of NO_2 VCDs without buffer screening as presented in Fig. 12b for the corresponding time series experiencing 0, 3, 5, 10 and 20 days of drought after Day 0. **(c)** The corresponding background time series of NO_2 VCDs with buffer screening as presented in Fig. 12c. **(d)** Differences between panels **(a)**, **(b)**. **(e)** Differences between panels **(a)**, **(c)**.

$65 \text{ ng N m}^{-2} \text{ s}^{-1}$ on the upper limit on Day 0. This is in line with findings from Jaeglé et al. (2004), who gave an estimate of $20 \text{ ng N m}^{-2} \text{ s}^{-1}$ for rain-induced sNO_x pulses in June in the Sahel. Furthermore, field studies suggest emission fluxes of nitrogen of about $2\text{--}60 \text{ ng N m}^{-2} \text{ s}^{-1}$ (Johansson and Sanhueza, 1988; Davidson, 1992a; Levine et al., 1996; Scholes et al., 1997), which covers our estimated upper and lower limits. Previous studies also note the strong dependence of soil emissions on temperature. We conducted initial tests using ECMWF soil temperature data (see Appendix F), but found no clear temperature dependence of sNO_x emissions. This is probably due to the systematic relation between temperature and the seasonal cycle, which affects the spatio-

temporal selection of the data, e.g. in April more southern pixels are selected and in June more northern pixels. In consequence, we indicate the need for more detailed investigation on how these pulsed emissions are affected by different soil temperatures.

After the first direct emission pulse, emissions remain at an enhanced level for a period of about 2 weeks as described in the previous chapter with approximately $3.3 \text{ ng N m}^{-2} \text{ s}^{-1}$ averaged over the Sahel. Analogous to the pulsed emission on Day 0, this value probably represents a lower limit because of the rather low spatial resolution of the extracted time series. These emissions are almost independent from the period of dry days after Day 0, which indicates that they are

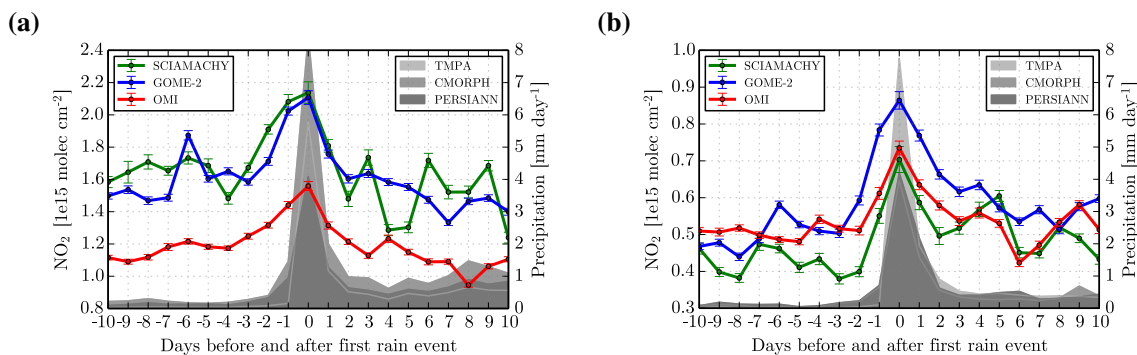


Figure 14. (a) NO₂ VCDs from SCIAMACHY, GOME-2 and OMI for south-western Africa in September–October–November around the first day of rainfall in this period. Precipitation is represented by the grey shaded areas. (b) Results for central Australia for the complete years 2007–2010.

potentially caused by the initial rain on Day 0 and not by subsequent precipitation the following days. Possible advection effects into or out of the considered pixels may thereby raise or lower the retrieved sNO_x fluxes. The analysis based on different dry phases after Day 0 also changes the probability for first rain events in pixels in close proximity. As we do not find strong differences in the emissions for different dry phases after Day 0, we conclude that the inflow of NO_x from adjacent pixels is not the dominant source for the enhancement after Day 0. In contrast, a systematic underestimation of the emissions is likely due to advection out of the central pixel. In sum, we estimate that the integrated emissions after Day 0 are potentially of the same order of magnitude as those from the first emission pulse on Day 0.

Peak emissions of sNO_x pulses typically occur on the scale of 1–3 days (Kim et al., 2012) in accordance to our results for the Sahel, South Africa and Australia showing peak emissions shortly after the first re-wetting. Some studies, on the other hand, measure peak emissions several days after the first re-wetting of the soil, e.g. 7 days as observed in field by Oikawa et al. (2015). Our algorithm does not specifically distinguish between such cases by taking average time series after the first precipitation event. Single pixels within the regions we investigated may exhibit peak emissions several days after the initial precipitation, which would, however, not be resolved by our analysis.

Our study focuses on the quantification of pulsed soil emissions and determines the NO₂ enhancement on Day 0 and the following days with respect to a sophisticatedly determined background. However, the seasonal pattern of the determined background, i.e. the NO₂ enhancement at the onset of raining season (compare Jaeglé et al., 2004), clearly indicates that it is mainly driven by microbial emissions from soils as well: from pulsed emissions discarded by our strict selection criteria or continuous emissions during wet season. Note that the seasonal pattern of NO₂ over the Sahel, as shown in Fig. 7, can neither be explained by biomass burning nor lightning. Figure 13c of the

manuscript shows that the background NO₂ VCDs are about 0.9×10^{15} molec cm⁻². This is about 0.17×10^{15} molec cm⁻² higher than background in winter. Thus, in addition to the pulsed emissions quantified above, a mean background of 0.17×10^{15} molec cm⁻² can be attributed to soil emissions as well. These estimates are based on TMPA precipitation data. For other precipitation products (CMORPH or PERSIANN), results change only slightly (see Appendix E).

In summary, we discriminate between soil emissions within: (a) 1–3 days (initial peak), (b) 14 days and (c) several months (background during the wet season). The separate quantification of soil emissions belonging to these three categories might also be adopted in model parametrizations of soil emissions. However, further research needs to be conducted on how these emission categories vary for different regions worldwide.

5.2 Seasonal soil nitrogen emissions in the Sahel

In this section we quantify the total soil emissions, both due to pulsed emissions and background, for the Sahel region. For the pulsed emissions on Day 0 (category a) and the following 2 weeks (b), the fluxes estimated above are multiplied by the area of the investigated region (0–30° E, 12–18° N). The statistics of our analysis in the Sahel suggest that on average one large pulsing event (after 60 days of drought) occurs within a single pixel in the April–May–June period. Scaling up the Day 0 emissions results in 1.2 and 12 GgN, considering the lower and upper flux estimates estimated above. Analogously, the emissions over the following 2 week period add up to 8.8 GgN. Together this sums up to 10.1–20.8 GgN emissions due to pulsing. As mentioned above, the observed increase of the background in the AMJ period of 0.17×10^{15} molec cm⁻² is mainly driven by microbial emissions from soils as well. When integrated over the complete April–May–June period, these seasonal soil emissions correspond to 46.4 GgN (again based on a NO_x lifetime of 4 h). Consequently, the emissions due to pulsing contribute about

21–44 % additionally to seasonal soil emissions for the Sahel and dominate the local NO_x concentrations on the particular days.

Jaeglé et al. (2004) determined top-down total soil emissions from GOME-2 measurements of about 400 GgN for North Equatorial Africa (0–18° N) in June alone. Our estimated total soil emissions of nitrogen (56.5–67.2 GgN for AMJ) are smaller, but are determined for a smaller region as well, which makes a direct comparison difficult.

5.3 Enhancements in NO₂ VCDs on Day –1

For all analysed study regions and individual grid pixels showing significant NO₂ spikes on Day 0, we also find enhancements in the NO₂ VCDs 1 to 2 days before the first day of rainfall. The phenomenon is especially pronounced for the study region in south-western Africa. The finding of enhanced NO₂ VCDs before Day 0 stands in contrast to the general expectation that soil emissions, e.g. of NO_x, are only caused by the initial rain event and the subsequent wetting of the soil. However, absolute humidity shows a steady increase several days before the first rain event. Thus, reasons for the early increase of NO₂ VCD may be an increase in atmospheric moisture content and dewfall, a misclassification of rainfall intensity by the precipitation algorithms, transport of NO₂ from neighbouring regions or spatial aliasing effects during the gridding of the satellite observations, i.e. the overlap of the ground footprint onto multiple grid boxes of the precipitation products. The latter two can occur if the ground pixel observed by the satellite overlaps with two or more grid pixels of the precipitation products or vice versa. This error is difficult to estimate, but should be more pronounced for larger satellite ground pixels, i.e. from SCIAMACHY, and less for instruments with smaller footprints, i.e. OMI. The fact that all instruments observe similar enhancements already on Day –1 indicates that this possible error source is not the dominant cause for the early increase in NO₂ VCDs. The use of three instruments for detecting NO₂, each having different overpass times during the day, also makes it less likely that a temporal mismatch of the precipitation and trace gas products, as described in the “Methodology” section, leads to the enhancements on Day –1.

In Fig. 5b it is shown that water vapour (H₂O) VCDs in the atmosphere retrieved by GOME-2 increases continuously for 10 days before the first precipitation event and peaks on Day –1. We speculate that the moist air over the extremely dry top soil layer induces initial sNO_x emissions, despite the fact that the soil is not directly wetted by rain. Also an enhanced dew formation and water adsorption potential, which are both important sources of water in semi-arid areas, have a major effect on microbiological activity (Verheye, 2008). The probability for nightly condensation over drying soils increases with higher absolute humidity. Although observations of these quantities are sparse, measurements in Israel, Jordan and in South Africa hint at contributions of 12 to

40 mm water per year in semi-arid regions (Verheye, 2008; Nicholson, 2011, and references therein). Transport of polluted air from the tropics northwards presumably also leads to enhanced NO₂ VCDs before Day 0. However, this effect is expected to be quite low as the enhancements before Day 0 are also seen for cases dominated by northerly winds coming from the Sahara, which are generally associated with lower NO₂ VCDs (see Fig. 11).

6 Conclusions

We have presented a top-down approach to infer rain-induced emission pulses of NO_x based on space-based measurements of NO₂. This is achieved by synchronizing time series at single grid pixels according to the first day of rain after a dry spell of prescribed duration. The method is applied globally and provides constraints on pulsed soil emissions of NO_x in regions where the NO_x budget is seasonally dominated by soil emissions. This approach is similar to Hudman et al. (2012), but extended by (a) performing the analysis globally with (b) high spatial resolution, and (c) keeping full track of the temporal evolution several weeks before and after a rain pulse with daily resolution. The latter was used to (d) perform a sophisticated background correction, which turned out to be necessary in order to account for the seasonal variations in the time series and allows to (e) quantify rain-induced soil emissions also beyond the strong peak on the first day of rain.

Sensitivity studies were conducted in order to (i) evaluate the impact of the a priori assumptions on thresholds for daily rainfall, i.e. the amount of precipitation and the required duration, (ii) investigate to what extent other NO_x sources like biomass burning or lightning NO_x might interfere and (iii) carefully check for possible retrieval artefacts (e.g. caused by clouds). None of these effects has shown to be critical for our conclusions.

Note, however, that our method was optimized for the quantification of pulsed soil emissions from space by demanding long droughts and good viewing conditions (low cloud fractions) on the day of precipitation onset. Thus, regions showing no clear response for these strict selections might still be capable of rain-induced soil emissions.

Strong peaks of enhanced NO₂ VCDs on the first day of rainfall after prolonged droughts are found in many semi-arid regions, in particular in the Sahel, south-western Africa, Australia and parts of India. A similar analysis for HCHO VCDs showed no indication for pulsed soil emissions. Closer inspection of the Sahel shows a strong dependence of precipitation-induced NO_x emissions on land type cover. This finding confirms similar results from laboratory measurements.

For the Sahel region, absolute enhancements of the NO₂ VCDs on the first day of rain based on OMI measurements 2007–2010 are on average 4×10^{14} molec cm⁻² and

exceed 1×10^{15} molec cm⁻² for individual grid cells. Results for SCIAMACHY and GOME-2 are comparable, and the slight differences can be primarily explained by different footprints, overpass times, cloud products, and retrieval schemes. Assuming a NO_x lifetime of 4 h, this corresponds to soil NO_x emissions in the range of $6 \text{ ng N m}^{-2} \text{ s}^{-1}$ up to $65 \text{ ng N m}^{-2} \text{ s}^{-1}$ on Day 0, in good agreement with literature values. Apart from the clear first-day peak, NO₂ VCDs are moderately enhanced (2×10^{14} molec cm⁻²) compared to background over the following 2 weeks suggesting potential further emissions during that period of about $3.3 \text{ ng N m}^{-2} \text{ s}^{-1}$. With respect to the seasonal NO_x budget, we assess a contribution between 21 to 44 % from these rain-induced intense pulsing events to total soil NO_x emissions in the Sahel.

In conclusion, our findings facilitate a detailed characterization and estimation of emission budgets for intense sNO_x pulses, triggered by individual rain events, which can improve parametrizations in modelling studies by dividing soil emissions into several parts: (i) pulsed emissions on short timescales, (ii) enhanced emissions after the initial pulse, and (iii) seasonal background emissions.

7 Data availability

All input data for this study are available online or upon request by the data producer. References for each product are provided in Sect. 2. The following list provides links to data products used within this study: NO₂ and HCHO column densities as well as cloud fractions (<http://www.temis.nl>), TRMM/TMPA precipitation (<https://pmm.nasa.gov/data-access/downloads/trmm>), CMORPH precipitation (http://www.cpc.ncep.noaa.gov/products/janowiak/cmorph_description.html), PERSIANN precipitation (<http://chrs.web.uci.edu/persiann/data.html>), ESA CCI soil moisture (<http://esa-soilmoisture-cci.org>), WWLLN lightning (<http://wwlln.net>), MODIS fire (<https://firms.modaps.eosdis.nasa.gov/download/>), ECMWF meteorology (<http://apps.ecmwf.int/datasets/>), GlobCover land cover (http://due.esrin.esa.int/page_globcover.php).

Appendix A: Reference case for different precipitation products as trigger

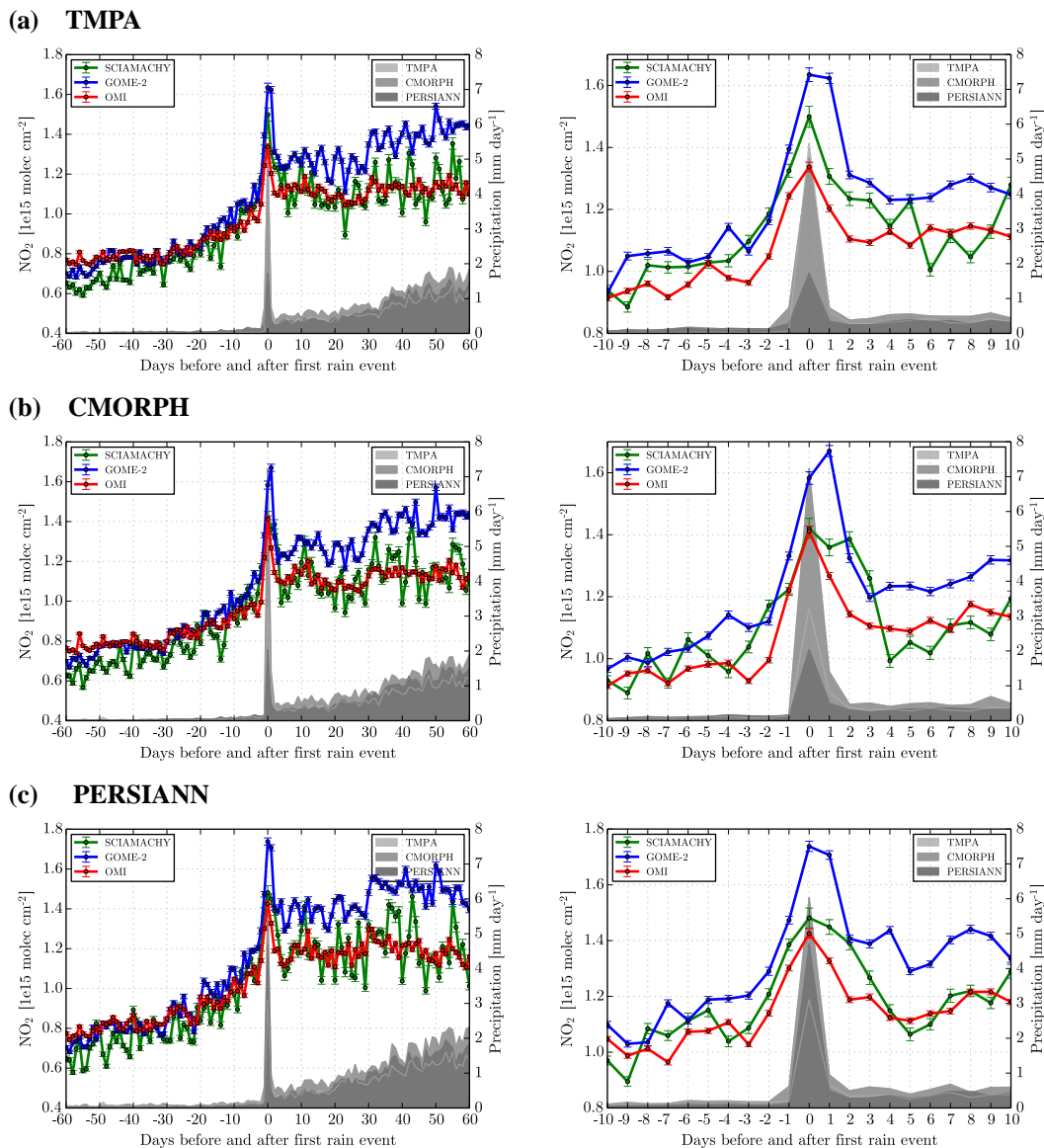


Figure A1. In this figure, NO_2 VCDs are shown (akin to Fig. 5e) from OMI (a), GOME-2 (b), SCIAMACHY (c) around the first day of rainfall for different precipitation products as trigger for the precipitation threshold of 2 mm for the Sahel region. The left panels represent the full time series of 60 days before and after Day 0, the right panels show a zoom-in for the 10 days before and after.

Appendix B: Different drought lengths for the reference case

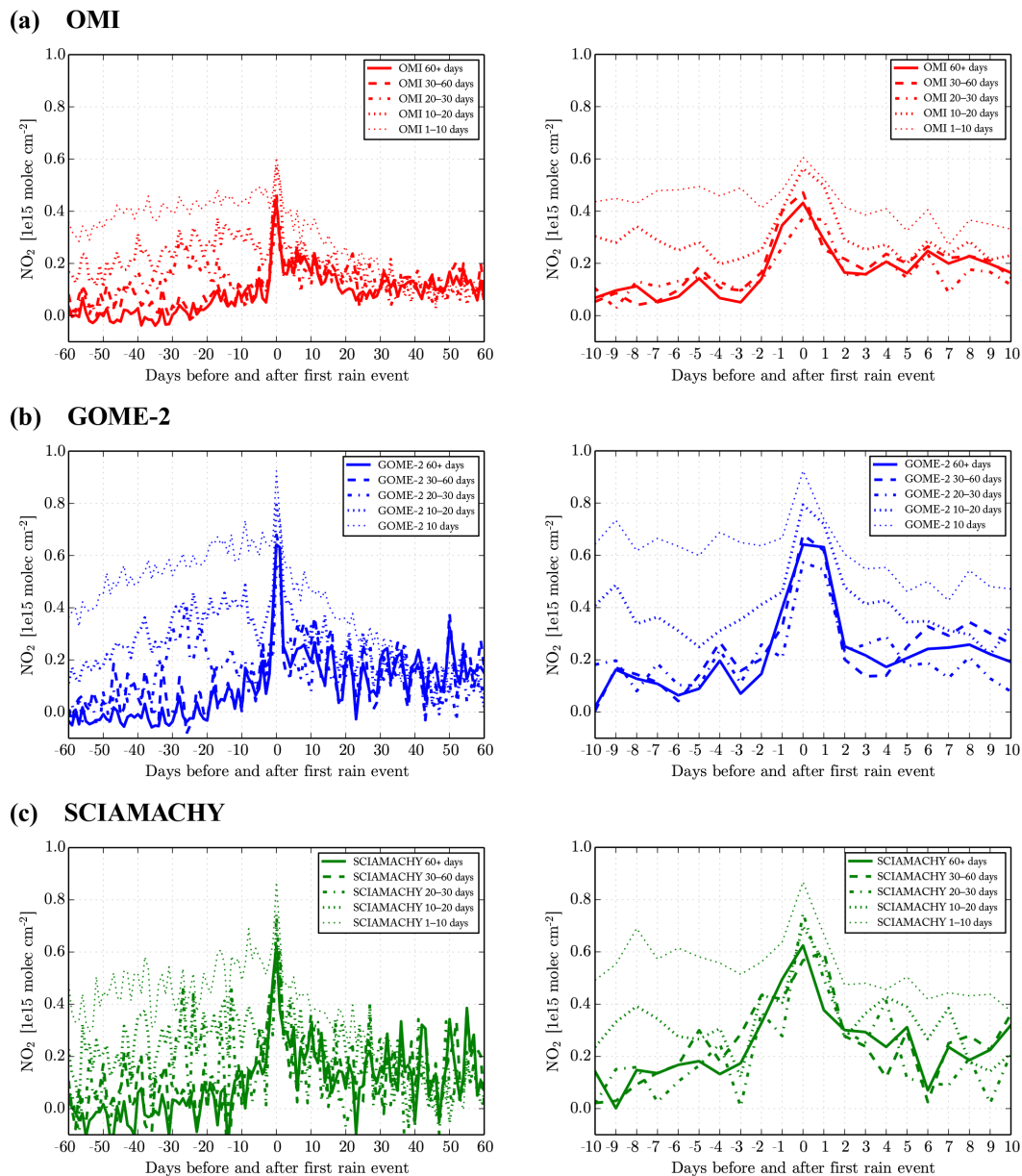


Figure B1. In this figure, NO₂ VCDs are shown from OMI (a), GOME-2 (b), SCIAMACHY (c) around the first day of rainfall for different preceding drought periods for the Sahel region with a precipitation threshold of 2 mm. For better intercomparison, the latitudinal background correction with buffer as described in Sect. 4.5 is applied to each time series individually. The left panels represent the full time series of 60 days before and after Day 0, the right panels show a zoom-in for the 10 days before and after.

Appendix C: Different precipitation thresholds on Day 0 for the reference case

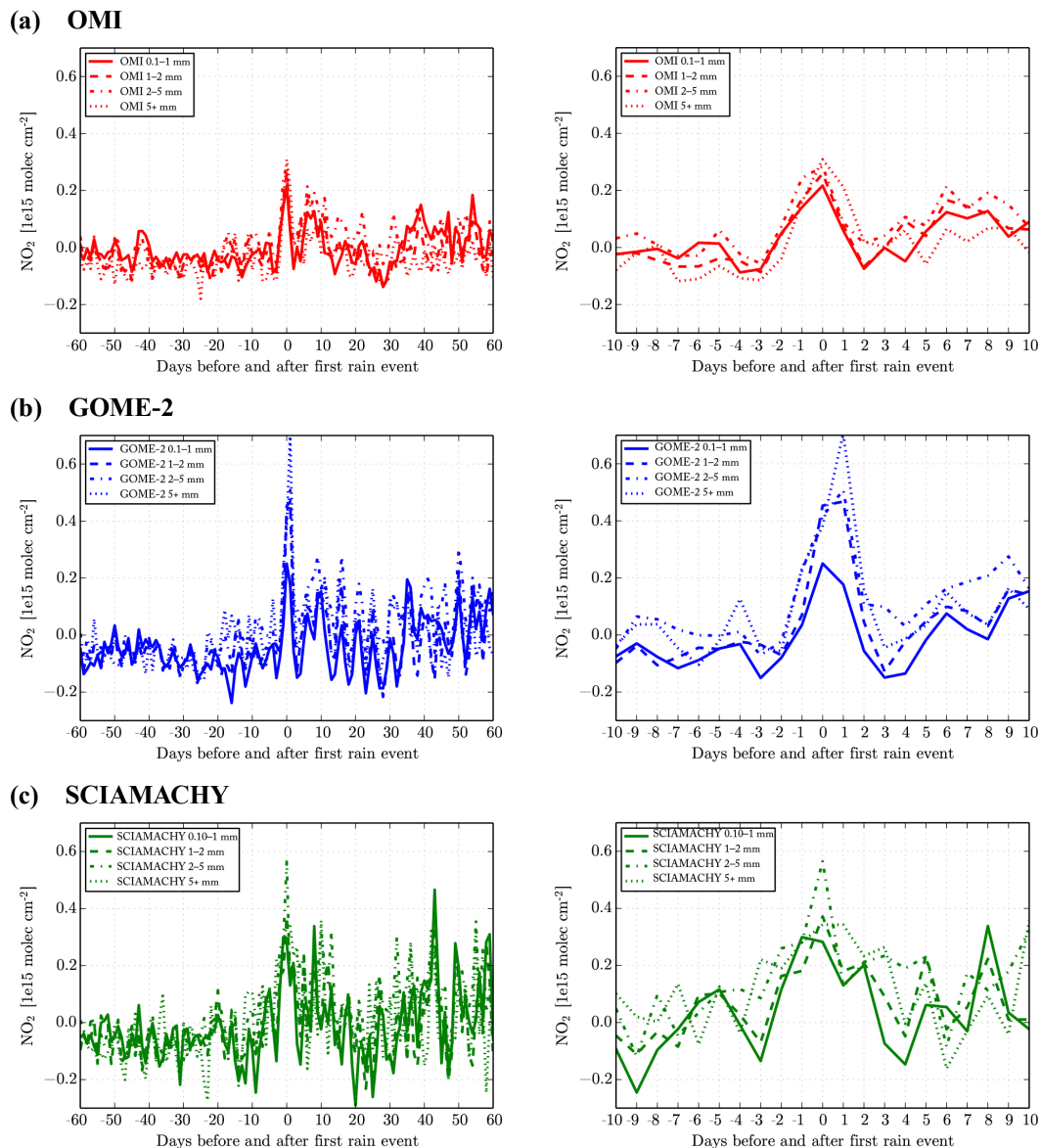


Figure C1. In this figure, NO_2 VCDs are shown from OMI (a), GOME-2 (b), SCIAMACHY (c) around the first day of rainfall for the Sahel region for a drought period of at least 60 days. The results are separated for different intervals of the precipitation threshold on Day 0. A drought day is defined by precipitation < 0.1 mm per day. For better intercomparison, the latitudinal background correction with buffer as described in Sect. 4.5 is applied to each time series individually. The left panels represent the full time series of 60 days before and after Day 0, the right panels show a zoom-in for the 10 days before and after.

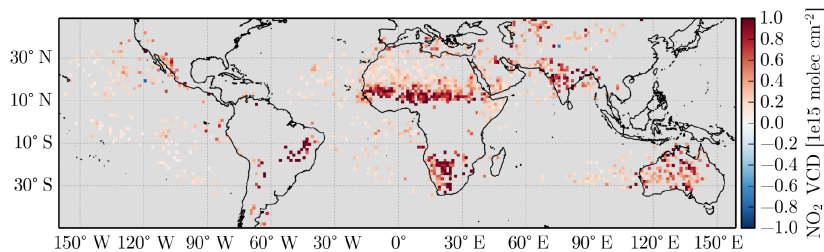
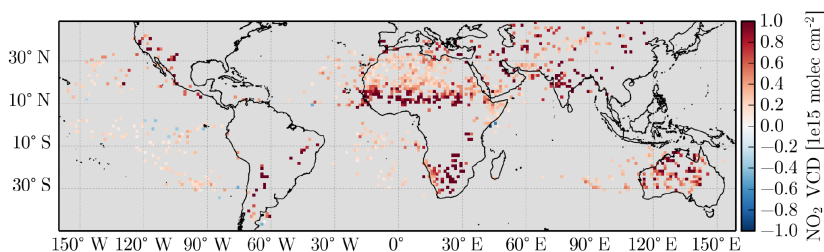
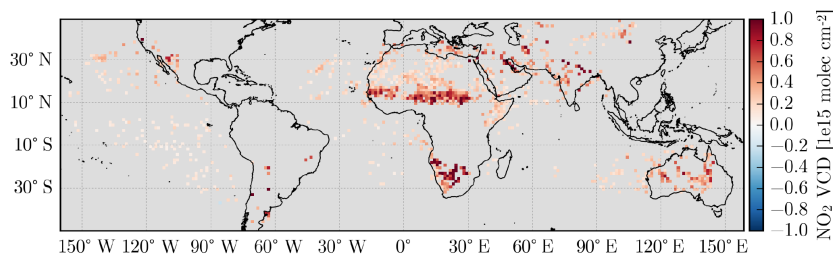
**Appendix D: Global maps for other satellite instruments
(60 days of drought, 2 mm precipitation threshold)****(a) GOME-2****(b) SCIAMACHY**

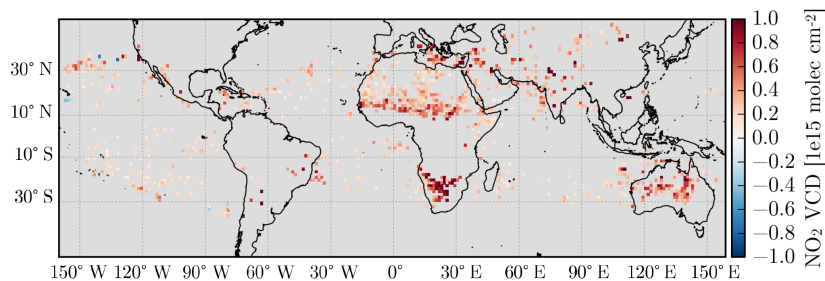
Figure D1. In this figure, absolute differences in NO_2 VCDs compared to Days -10 to -2 from GOME-2 **(a)** and SCIAMACHY **(b)** on Day 0 (first day of rainfall) are depicted, which were computed similarly as for OMI in Fig. 3d for OMI. The data were screened for significant changes and pixels containing less than 20 measurements on Day 0 (or less than 50 measurements from Day -10 to Day -2).

Appendix E: Impact of a priori precipitation product

(a) CMORPH



(b) PERSIANN



(c) Derived fluxes

	TRMM	CMORPH	PERSIANN
\emptyset Day0 enhanc. [$\text{ngNm}^{-2}\text{s}^{-1}$]	6.95	7.75	6.62
max. Day0 enhanc. [$\text{ngNm}^{-2}\text{s}^{-1}$]	64.61	64.61	64.61
Day1-14 enhanc. [$\text{ngNm}^{-2}\text{s}^{-1}$]	3.39	3.07	2.42
Background (soil) [$\text{ngNm}^{-2}\text{s}^{-1}$]	2.75	3.39	4.36
Background (total) [$\text{ngNm}^{-2}\text{s}^{-1}$]	14.54	15.18	16.15

Figure E1. In this figure, the impact of the precipitation product on the derived soil NO_x emissions is investigated. Panels (a, b) depict the NO_2 enhancement on Day 0 as in Fig. 3d, but based on CMORPH and PERSIANN data, respectively. While the absolute values differ for the Sahel, the final emission estimates for pulsed emissions are quite similar (see panel c), as the choice of the precipitation data affects the background correction as well.

Appendix F: Analysis for different soil temperatures

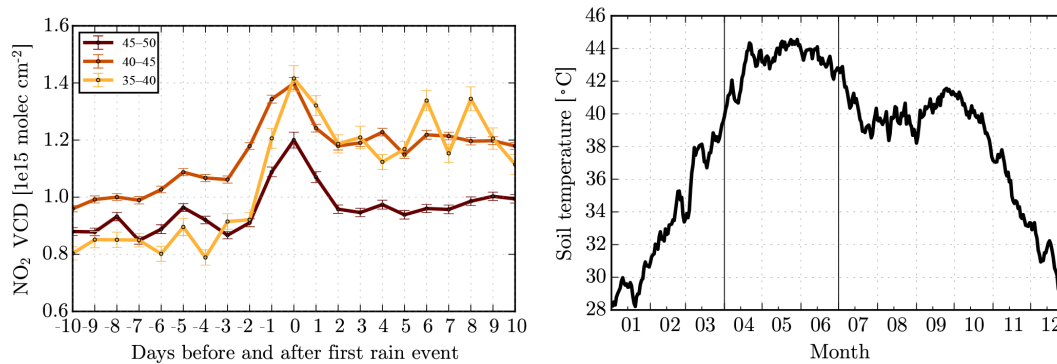


Figure F1. In this figure, NO₂ VCDs are shown (akin to Fig. 5e) from OMI around the first day of rainfall for different soil temperatures on Day 0 for the Sahel region (left panel). The right panel depicts daily time series of soil temperature (from 12:00 UTC ECMWF data) for the Sahel region (0–30° W, 12–18° N) averaged for the years 2007, 2008, 2009 and 2010.

Acknowledgements. The authors wish to thank the World Wide Lightning Location Network (<http://wwlln.net>), a collaboration among over 50 universities and institutions, for providing the lightning location data used in this paper. We acknowledge the free use of tropospheric NO₂ and HCHO column data from the GOME-2, SCIAMACHY and OMI sensors from <http://www.temis.nl> and would like to thank Isabelle De Smedt for providing the most recent version of the HCHO products. We thank also all other authors of data products used in this study for their efforts in producing and providing their data. Furthermore, we would like to thank Bettina Weber, Buhalgem Mamtimin and Franz X. Meixner for the inspiring and constructive discussions.

The article processing charges for this open-access publication were covered by the Max Planck Society.

Edited by: F. Boersma

Reviewed by: two anonymous referees

References

- Acarreta, J. R., De Haan, J. F., and Stammes, P.: Cloud pressure retrieval using the O₂-O₂ absorption band at 477 nm, *J. Geophys. Res.-Atmos.*, 109, D05204, doi:10.1029/2003JD003915, 2004.
- Arino, O., Gross, D., Ranera, F., Leroy, M., Bicheron, P., Brockman, C., Defourny, P., Vancutsem, C., Achard, F., Durieux, L., Bourg, L., Latham, J., Di Gregorio, A., Witt, R., Herold, M., Sambale, J., Plummer, S., and Weber, J. L.: GlobCover: ESA service for global land cover from MERIS, in: *Geoscience and Remote Sensing Symposium, 2007, IGARSS 2007, IEEE International*, 2412–2415, IEEE, 2007.
- Barger, N., Belnap, J., Ojima, D., and Mosier, A.: NO Gas Loss from Biologically Crusted Soils in Canyonlands National Park, Utah, *Biogeochemistry*, 75, 373–391, doi:10.1007/s10533-005-1378-9, 2005.
- Bassett, M. and Seinfeld, J. H.: Atmospheric equilibrium model of sulfate and nitrate aerosols, *Atmos. Environ.*, 17, 2237–2252, doi:10.1016/0004-6981(83)90221-4, 1983.
- Behrendt, T., Veres, P. R., Ashuri, F., Song, G., Flanz, M., Mamtimin, B., Bruse, M., Williams, J., and Meixner, F. X.: Characterisation of NO production and consumption: new insights by an improved laboratory dynamic chamber technique, *Biogeosciences*, 11, 5463–5492, doi:10.5194/bg-11-5463-2014, 2014.
- Bell, G., Halpert, M., Schnell, R., Higgins, R., Lawrimore, J., Kousky, V., Tinker, R., Thiaw, W., Chelliah, M., and Artusa, A.: Climate assessment for 1999, *B. Am. Meteorol. Soc.*, 81, 1328–1328, 2000.
- Belnap, J. and Lange, O.: *Biological Soil Crusts: Structure, Function, and Management*, Ecological studies, Springer, Berlin, 2001.
- Bertram, T., Heckel, A., Richter, A., Burrows, J. P., and Cohen, R. C.: Satellite measurements of daily variations in soil NO_x emissions, *Geophys. Res. Lett.*, 32, L24812, doi:10.1029/2005GL024640, 2005.
- Boersma, K., Jacob, D., Bucsela, E., Perring, A., Dirksen, R., van der A, R., Yantosca, R., Park, R., Wenig, M., Bertram, T., and Cohen, R.: Validation of OMI tropospheric NO₂ observations during INTEX-B and application to constrain emissions over the eastern United States and Mexico, *Atmos. Environ.*, 42, 4480–4497, doi:10.1016/j.atmosenv.2008.02.004, 2008.
- Boersma, K. F., Eskes, H. J., and Brinkma, E. J.: Error analysis for tropospheric NO₂ retrieval from space, *J. Geophys. Res.-Atmos.*, 109, D04311, doi:10.1029/2003JD003962, 2004.
- Boersma, K. F., Eskes, H. J., Veefkind, J. P., Brinkma, E. J., van der A, R. J., Sneep, M., van den Oord, G. H. J., Levelt, P. F., Stammes, P., Gleason, J. F., and Bucsela, E. J.: Near-real time retrieval of tropospheric NO₂ from OMI, *Atmos. Chem. Phys.*, 7, 2103–2118, doi:10.5194/acp-7-2103-2007, 2007.
- Boersma, K. F., Eskes, H. J., Dirksen, R. J., van der A, R. J., Veefkind, J. P., Stammes, P., Huijnen, V., Kleipool, Q. L., Sneep, M., Claas, J., Leitão, J., Richter, A., Zhou, Y., and Brunner, D.: An improved tropospheric NO₂ column retrieval algorithm for the Ozone Monitoring Instrument, *Atmos. Meas. Tech.*, 4, 1905–1928, doi:10.5194/amt-4-1905-2011, 2011.
- Boersma, K. F., Vinken, G. C. M., and Eskes, H. J.: Representativeness errors in comparing chemistry transport and chemistry climate models with satellite UV-Vis tropospheric column retrievals, *Geosci. Model Dev.*, 9, 875–898, doi:10.5194/gmd-9-875-2016, 2016.
- Bond, D., Steiger, S., Zhang, R., Tie, X., and Orville, R.: The importance of NO_x production by lightning in the tropics, *Atmos. Environ.*, 36, 1509–1519, doi:10.1016/S1352-2310(01)00553-2, 2002.
- Bontemps, S., Defourny, P., Van Bogaert, E., Arino, O., Kalogirou, V., Perez, R., and Julio, J.: GLOBCOVER 2009 – Products description and validation report, doi:10013/epic.39884.d016, Université catholique de Louvain (UCL) & European Space Agency (ESA), 2011.
- Bouwman, A., Boumans, L., and Batjes, N.: Emissions of N₂O and NO from fertilized fields: Summary of available measurement data, *Global Biogeochem. Cy.*, 16, 1058, doi:10.1029/2001GB001811, 2002.
- Bovensmann, H., Burrows, J. P., Buchwitz, M., Frerick, J., L, S. N., Rozanov, V. V., Chance, K. V., and Goede, A. P. H.: SCIAMACHY – Mission objectives and measurement modes, *J. Atmos. Sci.*, 56, 125–150, 1999.
- Burrows, J. P., Weber, M., Buchwitz, M., Rozanov, V., Ladstätter-Weißmayer, A., Richter, A., DeBeek, R., Hoogen, R., Bramstedt, K., Eichmann, K.-U., Eisinger, M., and Perner, D.: The Global Ozone Monitoring Experiment (GOME): Mission Concept and First Scientific Results, *J. Atmos. Sci.*, 56, 151–175, 1999.
- Callies, J., Corpaccioli, E., Eisinger, M., Hahne, A., and Lefebvre, A.: GOME-2 – METOP's second-generation sensor for operational ozone monitoring, *ESA Bull.*, 102, 28–36, 2000.
- Chameides, W. L., Fehsenfeld, F., Rodgers, M. O., Cardelino, C., Martinez, J., Parrish, D., Lonneman, W., Lawson, D. R., Rasmussen, R. A., Zimmerman, P., Greenberg, J., Middleton, P., and Wang, T.: Ozone precursor relationships in the ambient atmosphere, *J. Geophys. Res.-Atmos.*, 97, 6037–6055, doi:10.1029/91JD03014, 1992.
- Conrad, R.: Soil microorganisms as controllers of atmospheric trace gases (H₂, CO, CH₄, OCS, N₂O, and NO), *Microbiol. Rev.*, 60, 609–640, 1996.
- Crutzen, P.: Overview of tropospheric chemistry: Developments during the past quarter century and a look ahead, *Faraday Discuss.*, 100, 1–21, doi:10.1039/FD995000001, 1995.

- Crutzen, P. and Lelieveld, J.: Human Impacts on Atmospheric Chemistry, *Annu. Rev. Earth Planet. Sc.*, 29, 17–45, doi:10.1146/annurev.earth.29.1.17, 2001.
- Crutzen, P. J. and Andreae, M. O.: Biomass burning in the tropics - impact on atmospheric chemistry and biogeochemical cycles, *Science*, 250, 1669–1678, 1990.
- Davidson, E. A.: Pulses of Nitric Oxide and Nitrous Oxide Flux following Wetting of Dry Soil: An Assessment of Probable Sources and Importance Relative to Annual Fluxes, *Ecol. Bull.*, 42, 149–155, 1992a.
- Davidson, E. A.: Sources of Nitric Oxide and Nitrous Oxide following Wetting of Dry Soil, *Soil Sci. Soc. Am. J.*, 56, doi:10.2136/sssaj1992.03615995005600010015x, 1992b.
- De Smedt, I., Müller, J.-F., Stavrakou, T., van der A, R., Eskes, H., and Van Roozendaal, M.: Twelve years of global observations of formaldehyde in the troposphere using GOME and SCIAMACHY sensors, *Atmos. Chem. Phys.*, 8, 4947–4963, doi:10.5194/acp-8-4947-2008, 2008.
- De Smedt, I., Van Roozendaal, M., Stavrakou, T., Müller, J.-F., Lerot, C., Theys, N., Valks, P., Hao, N., and van der A, R.: Improved retrieval of global tropospheric formaldehyde columns from GOME-2/MetOp-A addressing noise reduction and instrumental degradation issues, *Atmos. Meas. Tech.*, 5, 2933–2949, doi:10.5194/amt-5-2933-2012, 2012.
- Dee, D. P., Uppala, S. M., Simmons, A. J., Berrisford, P., Poli, P., Kobayashi, S., Andrae, U., Balmaseda, M. A., Balsamo, G., Bauer, P., Bechtold, P., Beljaars, A. C. M., van de Berg, L., Bidlot, J., Bormann, N., Delsol, C., Dragani, R., Fuentes, M., Geer, A. J., Haimberger, L., Healy, S. B., Hersbach, H., Hølm, E. V., Isaksen, I., Kållberg, P., Köhler, M., Matricardi, M., McNally, A. P., Monge-Sanz, B. M., Morcrette, J.-J., Park, B.-K., Peubey, C., de Rosnay, P., Tavolato, C., Thépaut, J.-N., and Vitart, F.: The ERA-Interim reanalysis: configuration and performance of the data assimilation system, *Q. J. Roy. Meteor. Soc.*, 137, 553–597, doi:10.1002/qj.828, 2011.
- Delon, C., Galy-Lacaux, C., Boone, A., Lioussé, C., Serça, D., Adon, M., Diop, B., Akpo, A., Lavenu, F., Mougin, E., and Timouk, F.: Atmospheric nitrogen budget in Sahelian dry savannas, *Atmos. Chem. Phys.*, 10, 2691–2708, doi:10.5194/acp-10-2691-2010, 2010.
- Dowden, R., Brundell, J., and Rodger, C.: VLF lightning location by time of group arrival (TOGA) at multiple sites, *J. Atmos. Sol.-Terr. Phys.*, 64, 817–830, doi:10.1016/S1364-6826(02)00085-8, 2002.
- Ebert, E. E., Janowiak, J. E., and Kidd, C.: Comparison of Near-Real-Time Precipitation Estimates from Satellite Observations and Numerical Models, *B. Am. Meteorol. Soc.*, 88, 47–64, doi:10.1175/BAMS-88-1-47, 2007.
- Evans, R. and Ehleringer, J.: A break in the nitrogen cycles in aridlands? evidence from $\delta^{15}\text{N}$ of soils, *Oecologia*, 94, 314–317, doi:10.1007/BF00317104, 1993.
- Ganzeveld, L., Lelieveld, J., Dentener, F., Krol, M., Bouwman, A. J., and Roelofs, G.-J.: Global soil-biogenic NO_x emissions and the role of canopy processes, *J. Geophys. Res.*, 107, ACH 9-1–ACH 9-17, doi:10.1029/2001JD001289, 2002.
- Ghude, S. D., Lal, D. M., Beig, G., van der A, R., and Sable, D.: Rain-Induced Soil NO_x Emission From India During the Onset of the Summer Monsoon: A Satellite Perspective, *J. Geophys. Res.*, 115, D16304, doi:10.1029/2009JD013367, 2010.
- Giglio, L., Csizsar, I., and Justice, C. O.: Global distribution and seasonality of active fires as observed with the Terra and Aqua Moderate Resolution Imaging Spectroradiometer (MODIS) sensors, *J. Geophys. Res.*, 111, G02016, doi:10.1029/2005jg000142, 2006.
- Gloersen, P. and Barath, F. T.: A Scanning Multichannel Microwave Radiometer for Nimbus-G and SeaSat-A, *IEEE J. Oceanic Eng.*, 2, 172–178, 1977.
- Grossi, M., Valks, P., Loyola, D., Aberle, B., Slijkhuis, S., Wagner, T., Beirle, S., and Lang, R.: Total column water vapour measurements from GOME-2 MetOp-A and MetOp-B, *Atmos. Meas. Tech.*, 8, 1111–1133, doi:10.5194/amt-8-1111-2015, 2015.
- Hudman, R. C., Moore, N. E., Mebust, A. K., Martin, R. V., Russell, A. R., Valin, L. C., and Cohen, R. C.: Steps towards a mechanistic model of global soil nitric oxide emissions: implementation and space based-constraints, *Atmos. Chem. Phys.*, 12, 7779–7795, doi:10.5194/acp-12-7779-2012, 2012.
- Huffman, G. J., Bolvin, D. T., Nelkin, E. J., Wolff, D. B., Adler, R. F., Gu, G., Hong, Y., Bowman, K. P., and Stocker, E. F.: The TRMM Multisatellite Precipitation Analysis (TMPA): Quasi-Global, Multiyear, Combined-Sensor Precipitation Estimates at Fine Scales, *J. Hydrometeorol.*, 8, 38–55, doi:10.1175/JHM560.1, 2007.
- Jacob, D. J.: Introduction to Atmospheric Chemistry, Princeton University Press, 1999.
- Jaeglé, L., Martin, R. V., Chance, K., Steinberger, L., Kurosu, T. P., Jacob, D. J., Modi, A. I., Yoboué, V., Sigha-Nkamdjou, L., and Galy-Lacaux, C.: Satellite mapping of rain-induced nitric oxide emissions from soils, *J. Geophys. Res.-Atmos.*, 109, D21310, doi:10.1029/2004JD004787, 2004.
- Johansson, C. and Sanhueza, E.: Emission of NO from savanna soils during rainy season, *J. Geophys. Res.*, 93, 14193–14198, 1988.
- Joyce, R., Janowiak, J., Arkin, P., and Xie, P.: CMORPH: A method that produces global precipitation estimates from passive microwave and infrared data at high spatial and temporal resolution, *J. Hydrometeorol.*, 5, 487–503, 2004.
- Kaufman, Y. J., Justice, C. O., Flynn, L. P., Kendall, J. D., Prins, E. M., Giglio, L., Ward, D. E., Menzel, W. P., and Setzer, A. W.: Potential global fire monitoring from EOS-MODIS, *J. Geophys. Res.-Atmos.*, 103, 32215–32238, doi:10.1029/98JD01644, 1998.
- Kim, D.-G., Vargas, R., Bond-Lamberty, B., and Turetsky, M. R.: Effects of soil rewetting and thawing on soil gas fluxes: a review of current literature and suggestions for future research, *Biogeochemistry*, 9, 2459–2483, doi:10.5194/bg-9-2459-2012, 2012.
- Lay, E. H., Holzworth, R. H., Rodger, C. J., Thomas, J. N., Pinto, O., and Dowden, R. L.: WWLL global lightning detection system: Regional validation study in Brazil, *Geophys. Res. Lett.*, 31, L03102, doi:10.1029/2003GL018882, 2004.
- Lebel, T. and Ali, A.: Recent trends in the Central and Western Sahel rainfall regime (1990–2007), *J. Hydrol.*, 375, 52–64, doi:10.1016/j.jhydrol.2008.11.030, 2009.
- Levelt, P. F., van den Oord, B., Hilsenrath, E., Leppelmeier, G. W., Bhartia, P. K., Malkki, A., Kelder, H., van der A, R. J., Brinksma, E. J., van Oss, R., Veefkind, P., van Weele, M., and Noordhoek, R.: Science Objectives of EOS-Aura's Ozone Monitoring Instrument (OMI), Proceedings of the Quadrennial Ozone Symposium, Sapporo, 127–128, 2000.
- Levelt, P., van den Oord, G., Dobber, M., Malkki, A., Visser, H., de Vries, J., Stammes, P., Lundell, J., and Saari, H.: The ozone

- monitoring instrument, *IEEE T. Geosci. Remote.*, 44, 1093–1101, doi:10.1109/TGRS.2006.872333, 2006.
- Levine, J. S., Winstead, E. L., Parsons, D. A. B., Scholes, M. C., Scholes, R. J., Cofer III, W. R., Cahoon Jr., D. R., and Sebach, D. I.: Biogenic soil emissions of nitric oxide (NO) and nitrous oxide (N₂O) from savannas in South Africa: The impact of wetting and burning, *J. Geophys. Res.*, 101, 23689–23697, doi:10.1029/96JD01661, 1996.
- Liu, J., Duan, Z., Jiang, J., and Zhu, A.-X.: Evaluation of Three Satellite Precipitation Products TRMM 3B42, CMORPH, and PERSIANN over a Subtropical Watershed in China, *Adv. Meteorol.*, 2015, 151239, doi:10.1155/2015/151239, 2015.
- Ludwig, J., Meixner, F., Vogel, B., and Forstner, J.: Soil-air exchange of nitric oxide: an overview of processes, environmental factors, and modeling studies, *Biogeochemistry*, 52, 225–257, doi:10.1023/A:1006424330555, 2001.
- Martin, R.: Global inventory of nitrogen oxide emissions constrained by space-based observations of NO₂ columns, *J. Geophys. Res.*, 108, 4537, doi:10.1029/2003JD003453, 2003.
- Meixner, F. and Yang, W.: Biogenic emissions of nitric oxide and nitrous oxide from arid and semi-arid land, in: *Dryland Ecohydrology*, edited by: D'Odorico, P. and Porporat, A., 233–255, Springer, Dordrecht, 2006.
- Merry, R.: Acidity and alkalinity of soils, in: *Environmental and Ecological Chemistry, Encyclopedia of Life Support Systems*, UNESCO-EOLSS Publishers Paris, France, 2009.
- Monks, P. S.: Gas-phase radical chemistry in the troposphere, *Chem. Soc. Rev.*, 34, 376–395, doi:10.1039/B307982C, 2005.
- Munro, R., Eisinger, M., Anderson, C., Callies, J., Corpaccioli, E., Lang, R., Lefebvre, A., Livschitz, Y., and Albiñana, A. P.: GOME-2 on MetOp, in: *Proc. of The 2006 EUMETSAT Meteorological Satellite Conference*, Helsinki, Finland, 12–16 June 2006, EUMETSAT, p. 48, 2006.
- Munro, R., Lang, R., Klaes, D., Poli, G., Retscher, C., Lindstrot, R., Huckle, R., Lacan, A., Grzegorski, M., Holdak, A., Kokhanovsky, A., Livschitz, J., and Eisinger, M.: The GOME-2 instrument on the Metop series of satellites: instrument design, calibration, and level 1 data processing – an overview, *Atmos. Meas. Tech.*, 9, 1279–1301, doi:10.5194/amt-9-1279-2016, 2016.
- Nicholson, S. E.: *Dryland Climatology*, Cambridge University Press, doi:10.1017/CBO9780511973840, Cambridge Books Online, 2011.
- Novella, N. and Thiaw, W.: Validation of Satellite-Derived Rainfall Products over the Sahel, *Wyle Information Systems/CPC/NOAA*, 1–9, available at: https://www.eumetsat.int/website/wcm/idc/idcplg?IdcService=GET_FILE&dDocName=PDF_CONF_P55_S6_32_NOVELLA_P&RevisionSelectionMethod=LatestReleased&Rendition=Web (last access: 25 July 2016), 2010.
- Oikawa, P. Y., Ge, C., Wang, J., Eberwein, J. R., Liang, L. L., Allsman, L. A., Grantz, D. A., and Jenerette, G. D.: Unusually high soil nitrogen oxide emissions influence air quality in a high-temperature agricultural region, *Nat. Commun.*, 6, 8753, doi:10.1038/ncomms9753, 2015.
- Oswald, R., Behrendt, T., Ermel, M., Wu, D., Su, H., Cheng, Y., Breuninger, C., Moravek, A., Mougou, E., Delon, C., Loubet, B., Pommerening-Röser, A., Sörgel, M., Pöschl, U., Hoffmann, T., Andreae, M., Meixner, F., and Trebs, I.: HONO Emissions from Soil Bacteria as a Major Source of Atmospheric Reactive Nitrogen, *Science*, 341, 1233–1235, doi:10.1126/science.1242266, 2013.
- Palmer, P. I., Jacob, D. J., Chance, K., Martin, R. V., Spurr, R. J. D., Kurosu, T. P., Bey, I., Yantosca, R., Fiore, A., and Li, Q.: Air mass factor formulation for spectroscopic measurements from satellites: Application to formaldehyde retrievals from the Global Ozone Monitoring Experiment, *J. Geophys. Res.-Atmos.*, 106, 14539–14550, doi:10.1029/2000JD900772, 2001.
- Pfieferth, U., Trentmann, J., Fink, A. H., and Ahrens, B.: Evaluating Satellite-Based Diurnal Cycles of Precipitation in the African Tropics, *J. Appl. Meteorol. Clim.*, 55, 23–39, doi:10.1175/JAMC-D-15-0065.1, 2016.
- Pilegaard, K.: Processes regulating nitric oxide emissions from soils, *Philos. T. R. Soc. B*, 368, 20130126, doi:10.1098/rstb.2013.0126, 2013.
- Pipunic, R. C., Ryu, D. R., Costelloe, J., and Su, C.-H.: Evaluation of real-time satellite rainfall products in semi-arid/arid Australia, in: *MODSIM2013*, edited by: Piantadosi, J., Anderssen, R. S., and Boland, J., 3106–3112, Australia Modelling & Simulation Society of Australia & New Zealand, Canberra, Australia, 2013.
- Platt, U. and Stutz, J.: *Differential Optical Absorption Spectroscopy: Principles and Applications*, Physics of Earth and Space Environments Series, Springer-Verlag Berlin Heidelberg, 2008.
- Rast, M., Bezy, J. L., and Bruzzi, S.: The ESA Medium Resolution Imaging Spectrometer MERIS a review of the instrument and its mission, *Int. J. Remote. Sens.*, 20, 1681–1702, doi:10.1080/014311699212416, 1999.
- Richter, A. and Burrows, J.: Retrieval of Tropospheric NO₂ from GOME Measurements, *Adv. Space Res.*, 29, 1673–1683, 2002.
- Rodger, C. J., Werner, S., Brundell, J. B., Lay, E. H., Thomson, N. R., Holzworth, R. H., and Dowden, R. L.: Detection efficiency of the VLF World-Wide Lightning Location Network (WWLLN): initial case study, *Ann. Geophys.*, 24, 3197–3214, doi:10.5194/angeo-24-3197-2006, 2006.
- Romilly, T. G. and Gebremichael, M.: Evaluation of satellite rainfall estimates over Ethiopian river basins, *Hydrol. Earth Syst. Sci.*, 15, 1505–1514, doi:10.5194/hess-15-1505-2011, 2011.
- Schlecht, E. and Hiernaux, P.: Beyond adding up inputs and outputs: process assessment and upscaling in modelling nutrient flows, *Nutr. Cycl. Agroecosys.*, 70, 303–319, 2004.
- Scholes, M., Martin, R., Scholes, R., Parsons, D., and Winstead, E.: NO and N₂O emissions from savanna soils following the first simulated rains of the season, *Nutr. Cycl. Agroecosys.*, 48, 115–122, doi:10.1023/a:1009781420199, 1997.
- Schumann, U. and Huntrieser, H.: The global lightning-induced nitrogen oxides source, *Atmos. Chem. Phys.*, 7, 3823–3907, doi:10.5194/acp-7-3823-2007, 2007.
- Seinfeld, J. H. and Pandis, S. N.: *Atmospheric Chemistry and Physics: From Air Pollution to Climate Change*, Wiley-Interscience, 2nd Edn., Hoboken, New Jersey, 2006.
- Simpson, J., Kummerow, C., Tao, W., and Adler, R.: On the Tropical Rainfall Measuring Mission (TRMM), *Meteorol. Atmos. Phys.*, 60, 19–36, 1996.
- Solomon, S., Schmeltekopf, A. L., and Sanders, R. W.: On the interpretation of zenith sky absorption measurements, *J. Geophys. Res.*, 92, 8311–8319, 1987.

- Sorooshian, S., Hsu, K.-L., and Gao, X.: Evaluation of PERSIANN System Satellite-Based Estimates of Tropical Rainfall, *B. Am. Meteorol. Soc.*, 81, 2035–2046, 2000.
- Steinkamp, J. and Lawrence, M. G.: Improvement and evaluation of simulated global biogenic soil NO emissions in an AC-GCM, *Atmos. Chem. Phys.*, 11, 6063–6082, doi:10.5194/acp-11-6063-2011, 2011
- Steinkamp, J., Ganzeveld, L. N., Wilcke, W., and Lawrence, M. G.: Influence of modelled soil biogenic NO emissions on related trace gases and the atmospheric oxidizing efficiency, *Atmos. Chem. Phys.*, 9, 2663–2677, doi:10.5194/acp-9-2663-2009, 2009.
- van Groenigen, J. W., Huygens, D., Boeckx, P., Kuypers, Th. W., Lubbers, I. M., Rütting, T., and Groffman, P. M.: The soil N cycle: new insights and key challenges, *SOIL*, 1, 235–256, doi:10.5194/soil-1-235-2015, 2015.
- Veefkind, J., Aben, I., McMullan, K., Förster, H., de Vries, J., Oter, G., Claas, J., Eskes, H., de Haan, J., Kleipool, Q., van Weele, M., Hasekamp, O., Hoogeveen, R., Landgraf, J., Snel, R., Tol, P., Ingmann, P., Voors, R., Kruizinga, B., Vink, R., Visser, H., and Levelt, P.: TROPOMI on the ESA Sentinel-5 Precursor: A GMES mission for global observations of the atmospheric composition for climate, air quality and ozone layer applications, *Remote Sens. Environ.*, 120, 70–83, doi:10.1016/j.rse.2011.09.027, 2012.
- Veres, P. R., Behrendt, T., Klapthor, A., Meixner, F. X., and Williams, J.: Volatile Organic Compound emissions from soil: using Proton-Transfer-Reaction Time-of-Flight Mass Spectrometry (PTR-TOF-MS) for the real time observation of microbial processes, *Biogeosciences Discuss.*, 11, 12009–12038, doi:10.5194/bgd-11-12009-2014, 2014.
- Verhey, W.: Soils of arid and semi arid regions, in: Land use, land cover and soil sciences, edited by: Verhey, W. H., *Encyclopedia of Life Support Systems (EOLSS)*, UNESCO-EOLSS Publishers, Paris, France, 2008.
- Vinken, G. C. M., Boersma, K. F., Maasackers, J. D., Adon, M., and Martin, R. V.: Worldwide biogenic soil NO_x emissions inferred from OMI NO₂ observations, *Atmos. Chem. Phys.*, 14, 10363–10381, doi:10.5194/acp-14-10363-2014, 2014.
- Virginia, R., Jarrell, W., and Franco-Vizcaino, E.: Direct measurement of denitrification in a Prosopis (Mesquite) dominated Sonoran Desert ecosystem, *Oecologia*, 53, 120–122, doi:10.1007/BF00377145, 1982.
- Wagner, T., Heland, J., Zöger, M., and Platt, U.: A fast H₂O total column density product from GOME – Validation with in-situ aircraft measurements, *Atmos. Chem. Phys.*, 3, 651–663, doi:10.5194/acp-3-651-2003, 2003.
- Wagner, T., Beirle, S., Grzegorski, M., and Platt, U.: Global trends (1996–2003) of total column precipitable water observed by Global Ozone Monitoring Experiment (GOME) on ERS-2 and their relation to near-surface temperature, *J. Geophys. Res.-Atmos.*, 111, d12102, doi:10.1029/2005JD006523, 2006.
- Wagner, W., Dorigo, W., Jeu, R. D., Fernandez, D., Benveniste, J., Haas, E., Ertl, M., Sensing, R., Amsterdam, V. U., Sciences, G.-E., Agency, E. S., Galilei, V. G., Systems, G. I., and Cycle, W.: Fusion of active and passive microwave observations to create an Essential Climate Variable data record on soil moisture, *ISPRS Annals of the Photogrammetry, Remote Sensing and Spatial Information Sciences*, I-7, 315–321, 2012.
- Wang, L., Manzoni, S., Ravi, S., Riveros-Iregui, D., and Caylor, K.: Dynamic interactions of ecohydrological and biogeochemical processes in water-limited systems, *Ecosphere*, 6, 1–27, doi:10.1890/ES15-00122.1, 2015.
- Wang, P., Stammes, P., van der A, R., Pinardi, G., and van Roozendael, M.: FRESCO+: an improved O₂ A-band cloud retrieval algorithm for tropospheric trace gas retrievals, *Atmos. Chem. Phys.*, 8, 6565–6576, doi:10.5194/acp-8-6565-2008, 2008.
- Wang, Y., McElroy, M. B., Martin, R. V., Streets, D. G., Zhang, Q., and Fu, T.-M.: Seasonal variability of NO_x emissions over east China constrained by satellite observations: Implications for combustion and microbial sources, *J. Geophys. Res.-Atmos.*, 112, D06301, doi:10.1029/2006JD007538, 2007.
- Warneck, P. and Williams, J.: *The Atmospheric Chemist's Companion: Numerical Data for Use in the Atmospheric Sciences*, Springer, Berlin, 2012.
- Weber, B., Wu, D., Tamm, A., Ruckteschler, N., Rodríguez-Caballero, E., Steinkamp, J., Meusel, H., Elbert, W., Behrendt, T., Sörgel, M., Cheng, Y., Crutzen, P. J., Su, H., and Pöschl, U.: Biological soil crusts accelerate the nitrogen cycle through large NO and HONO emissions in drylands, *P. Natl. Acad. Sci. USA*, 112, 15384–15389, doi:10.1073/pnas.1515818112, 2015.
- Wentz, F. and Spencer, R.: SSM/I Rain Retrievals within a Unified All-Weather Ocean Algorithm, *J. Atmos. Sci.*, 55, 1613–1627, 1998.
- Wentz, F., Ashcroft, P., and Gentemann, C.: Post-Launch Calibration of the TRMM Microwave Imager, *IEEE T. Geosci. Remote*, 39, 415–422, 2001.
- Wentz, F. J.: SSM/I Version-7 Calibration Report, Remote Sensing Systems, Santa Rosa, CA, available at: http://images.remss.com/papers/rsstech/2012_011012_Wentz_Version-7_SSMI_Calibration.pdf (last access: 25 July 2016), 2013.
- Williams, E. J., Parrish, D. D., and Fehsenfeld, F. C.: Determination of nitrogen oxide emissions from soils: Results from a grassland site in Colorado, United States, *J. Geophys. Res.-Atmos.*, 92, 2173–2179, doi:10.1029/JD092iD02p02173, 1987.
- Williams, E. J., Hutchinson, G. L., and Fehsenfeld, F. C.: NO_x And N₂O Emissions From Soil, *Global Biogeochem. Cy.*, 6, 351–388, doi:10.1029/92GB02124, 1992.
- Yienger, J. J. and Levy, H.: Empirical model of global soil-biogenic NO_x emissions, *J. Geophys. Res.*, 100, 11447–11464, 1995.
- Zhao, C. and Wang, Y.: Assimilated inversion of NO_x emissions over east Asia using OMI NO₂ column measurements, *Geophys. Res. Lett.*, 36, L06805, doi:10.1029/2008GL037123, 2009.